

The X-SERVS Survey: New *XMM-Newton* Source Catalog for the XMM-LSS field

C.-T. J. Chen^{1*}, W. N. Brandt, B. Luo, P. Ranalli, and Friends
¹*PSU*

Accepted XXX. Received YYY; in original form ZZZ

ABSTRACT

We present source catalogs from the XMM-Spitzer Extragalactic Representative Volume Survey in the XMM-Large Scale Structure survey region (X-SERVS:XMM-LSS). The survey is comprised of 1.1 Ms new *XMM-Newton* AO-15 data and 1.6 Ms archival data, totaling 2.7 Ms flare-filtered exposure over a 5.3 deg² area. We provide X-ray catalogs of 5218 sources detected in the soft (0.5–2 keV), hard (2–10 keV), and full (0.5–10 keV) bands. Sources are first detected using *XMM-Newton* SAS task EWAVELET with THRESHOLD > 4 and further verified by the SAS task EMLDETECT with DET_ML > 6, which is equivalent to a false-detection probability of $P = 0.0025$. A total of 2375 new X-ray sources are detected compared to the XMM-XXL-North survey in the same area. Our flux limits and distributions are comparable to those of the XMM-COSMOS survey. The median fluxes at the soft, hard, and full bands (in erg cm⁻² s⁻¹) are 2.65×10^{-15} , 1.48×10^{-14} , and 8.78×10^{-15} , respectively. As confirmed using available *Chandra* sources over $\approx 5\%$ of XMM-LSS, we identified multiwavelength counterparts that are 97% reliable in the central 4.5 deg² region covered by *Spitzer* SERVS. For the full 5.3 deg² region the reliability is > 94%. Results of multiwavelength identifications are also included in the source catalog, along with basic optical-to-infrared photometry as well as spectroscopic redshifts from the publicly available surveys.

Key words: keyword1 – keyword2 – keyword3

1 INTRODUCTION

PLACE HOLDER

2 XMM-NEWTON OBSERVATIONS IN THE XMM-LSS REGION AND DATA REDUCTION

2.1 *XMM-Newton* data in the XMM-LSS region

The XMM-LSS field has been targeted by a number of *XMM-Newton* surveys of different sensitivities. The original XMM-LSS survey was a ≈ 11 deg² field typically covered by observations of ≈ 10 ks exposure time per pointing, each separated by 20' (Pacaud et al. 2006; Pierre et al. 2016). Within the 11 deg² field, ≈ 4 deg² were also observed by the *XMM-Newton* Medium Deep Survey (XMDS, 20–25 ks exposure depth, Chiappetti et al. 2005). In addition, the Subaru *XMM-Newton* Deep Survey (SXDS, Ueda et al. 2008), adjacent to the XMDS field, covers a 1.14 deg² area with and

reaches ≈ 50 ks exposure per pointing (Ueda et al. 2008). Moreover, the XMM-LSS field recently became a part of the 25 deg² XMM-XXL-North field (Pierre et al. 2016), which has similar *XMM-Newton* coverage as the original XMM-LSS survey.

In addition to the X-ray data, XMM-LSS is among the extragalactic fields with the extensive multiwavelength coverage. In particular, the central ≈ 5 deg² area of the XMM-XXL-North field (i.e., the combination of XMDS and SXDS fields) is covered uniformly by multiple photometric and spectroscopic surveys (see Sec. 5 for more details). Compared to the multiwavelength data, archival *XMM-Newton* observations covering this sky region span a wide range of exposure time (10–100 ks). In order to improve the non-uniform *XMM-Newton* coverage compared to the multiwavelength data in this field, we obtained *XMM-Newton* AO-15 observations taken between July 2016 to February 2017 with a total of 1.3 Ms exposure time. Our AO-15 data include 67 *XMM-Newton* observations covering the majority of the XMM-LSS survey region. In addition to the new data, we made use of all the overlapping archival *XMM-Newton* observations to create a deep *XMM-Newton* catalog contiguously covering most of the SERVS data in the XMM-LSS re-

* E-mail: ctchen@psu.edu

Table 1. The *XMM-Newton* data used to create the source catalog include 153 observations with a total of 2.7 Ms of background-screened exposure time (MOS1), of which 1.1 Ms is from the new AO–15 observations. Columns from left to right: target field, *XMM-Newton* revolution, *XMM-Newton* ObsID, observation starting time, Right Ascension and Declination (J2000), background-screened good-time-interval (GTI) exposure time for PN, MOS1, and MOS2. This table is available in its entirety online.

Field	Revolution	ObsID	Date (UT)	R.A.	Decl.	GTI (PN) (ks)	GTI (MOS1) (ks)	GTI (MOS2) (ks)
AO-15	3054	0780450101	2016-08-13T01:34:06	35.81072	-5.15989	20.91	23.61	23.61
XMM-LSS	1205	0404965101	2006-07-09T08:08:08	35.80953	-5.48532	3.44	10.36	9.91
XMDS	287	0111110401	2001-07-03T14:01:54	35.97582	-5.15253	21.40	27.20	27.40
SXDS	118	0112370101	2000-07-31T21:57:54	34.47819	-4.98115	39.13	42.70	42.83
XMM-XXL-N	2137	0677580101	2011-08-10T01:53:35	38.00217	-4.49993	4.94	5.93	5.52
XLSSJ022404.0-041328	0928	0210490101	2005-01-01T19:08:30	36.03267	-4.20230	80.28	87.98	87.98

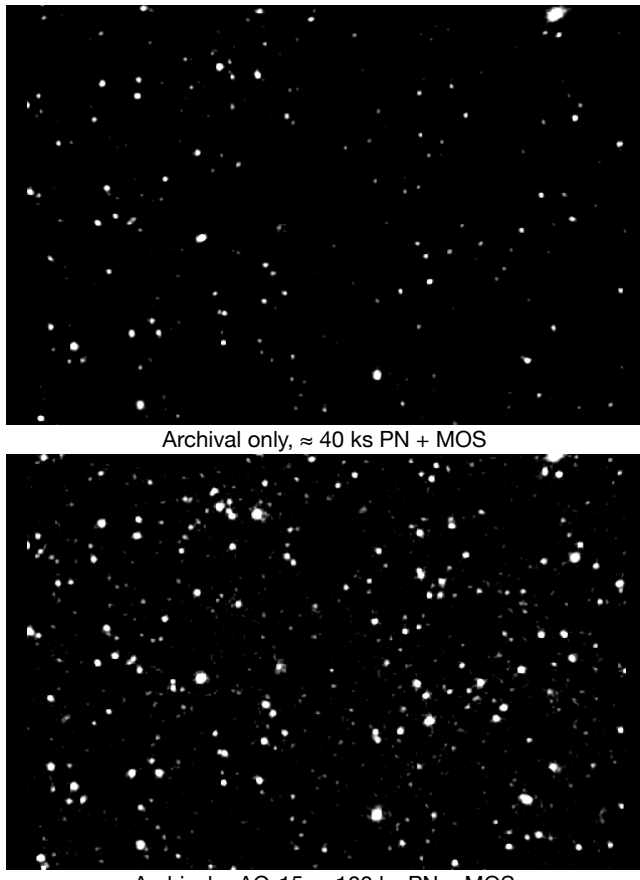


Figure 1. Top – Background-subtracted, smoothed image at the 0.5–10 keV band for a 0.8×0.6 deg 2 region centered at RA = 35.58 $^\circ$, DEC = −4.965 $^\circ$. This image is created using only the archival data. Bottom – Same as the top image, but all archival data and the new AO-15 data are included. The typical exposure values can also be found in Fig. 2.

After excluding observations that were completely lost due to flaring background (see §2.2), the archival data used here include 51 observations culled from the 10 ks XMM-LSS survey, eighteen 20–25 ks observations from XMDS, 4 mosaic-mode observations¹ obtained as part of the XMM-XXL survey (Pierre et al. 2016), 4 archival *XMM-Newton*

¹ Each mosaic-mode observation is comprised of \approx ten 10 ks exposures.

observations targeting galaxy clusters identified in the XXL and LSS surveys (≈ 30 –100 ks), and the ten 50 ks observations from SXDS. We present the details of each observation in Table 1.

Our AO-15 observations were separated into two epochs to minimize the effects of background flaring. We first observed the XMM-LSS sky-region in the SERVS footprint with ≈ 1 Ms *XMM-Newton* exposure time during July–August 2016. We then screened these first observations for flaring backgrounds (§2.2) and re-observed the background contaminated sky-regions using the remaining 0.3 Ms. Notably, we also observed the SXDS region in which one of the SXDS observations carried out in 2002 was severely affected by background flares. In this work, we present an X-ray catalog obtained from a 5.3 deg 2 sky-region with $34.2^\circ < \text{RA} < 37.125^\circ$ and $-5.72 < \text{Dec} < -3.87$. The sky-region is primarily selected by the footprint of our AO-15 observations, with additional SXDS data within the SERVS footprint in the corner. A total of ≈ 3 Ms of *XMM-Newton* observations is used for generating the X-ray catalog. In Fig. 1, we show the background-subtracted, 0.5–10 keV image (see §3 for the details of data analysis) from a ≈ 0.5 deg 2 region in XMM-LSS generated using the combined AO-15 and archival data. An image generated using only the archival data is also shown for comparison.

2.2 Data preparation and background flare filtering

We used the *XMM-Newton* Science Analysis System (SAS) 16.1.0 and HEASOFT 6.21 for our data analysis. The *XMM-Newton* Observation Data Files (ODFs) were processed with the SAS tasks EPICPROC (EPPROC and EMPROC for PN and MOS, respectively) to create MOS1, MOS2, PN, and PN out-of-time (OOT) event files for each ObsID. For observations taken in mosaic mode or with unexpected interruptions due to strong background flares, we use the SAS task EMOSAIC_PREP to separate the event files into individual pseudo-exposures and assign pseudo exposure IDs.² For the mosaic

² For mosaic-mode observations, multiple exposures are stored in a single event file for each EPIC camera after ODF processing. EMOSAIC_PREP separates the single event file into multiple pseudo event files with the same ObsID but different EXP_ID and EXPIDSTR, which are informative FITS file keywords required by the SAS tasks. For observations with unexpected interruptions, the exposure is separated into multiple event files with the same ObsID and EXP_ID by EPICPROC, but with different EXPIDSTR.

mode observations, we also determine the RA/DEC of each pseudo-exposure using the AHFRA and AHFDEC values in the attitude files created using the SAS task ATTHKGGEN.

For each event file, we create single event light curves in time bins of 100 s for high (10–12 keV) and low (0.3–10 keV) energies using EVSELECT to search for time intervals without significant background flares (the “good time intervals”, GTIs). We first remove time intervals with 10–12 keV count rates exceeding 3σ above the mean, and then repeat the 3σ clipping procedure for the low-energy light curves. Since the background flares usually manifest as a high-count-rate tail in addition to the Gaussian-shape count-rate histogram, adopting the 3σ clipping rule can effectively remove the high-count-rate tail while retaining useful scientific data. For a small number of event files with intense background flares, we instead filter the event files using the nominal count rate thresholds suggested by the *XMM-Newton* Science Operations Centre.³ Observations with $\text{GTI} < 2 \text{ ks}$ are discarded. A total of 2.7 Ms exposure remains after flare filtering, including 1.1 Ms from AO 15 and 1.6 Ms from the archival data. After screening for background flares, we further exclude events in energy ranges that overlap with the instrumental background lines (Al K α lines at 1.45–1.54 keV for MOS and PN; Cu lines at 7.2–7.6 keV and 7.8–8.2 keV for PN).

From the background-screened, instrumental-line-removed event files, we extract images with a 4'' pixel size using EVSELECT⁴ in the following bands: 0.5–2 (soft) keV and 2–10 keV (hard), and 0.5–10 keV (full) bands. For each image, we generate exposure maps with and without vignetting-corrections using the SAS task EEXPMAP. We set USEFASTPIXELIZATION=0 and ATTREBIN=0.5 in order to obtain more accurate exposure maps. Detector masks were also generated using the SAS task EMASK. We show the distribution of exposure values across the XMM-LSS field and the PN+MOS exposure map in Fig. 2

3 THE MAIN X-RAY SOURCE CATALOG

3.1 First-pass source detection and astrometric correction

The astrometric accuracy of *XMM-Newton* observations can be affected by the pointing uncertainties of *XMM-Newton*. This uncertainty is usually smaller than a few arcsecs, but can be as large as $\approx 10''$ (e.g., Cappelluti et al. 2007; Watson et al. 2008; Rosen et al. 2016). To achieve better astrometric accuracy and to minimize any systematic offsets between different *XMM-Newton* observations, we run an initial pass of source detection for each observation and then use the first-pass source list to register the *XMM-Newton* observations onto a common WCS frame. The first-pass source detection methods are outlined below:

values. EMOSAIC_PREP assigns a separate EXP_ID for each event file, which is necessary for SAS source-detection tasks.

³ <https://www.cosmos.esa.int/web/xmm-newton/sas-thread-epic-filterbackground>

⁴ The 4'' pixel size is set by the parameter IMAGEBINSIZE= 80 in the SAS task EVSELECT.

- (i) For the exposure taken by each instrument for each observation, we generate a temporary source list using the SAS task EWAVELET with a low likelihood threshold (THRESHOLD=4). EWAVELET is a wavelet-based algorithm that runs on the count-rate image generated using the image and exposure map extracted as described in §2.2.
- (ii) We use the temporary source list as an input to generate background images using the SAS task ESPLINEMAP with METHOD=MODEL. The METHOD=MODEL option of ESPLINEMAP fits the source-excised image with two templates: the vignetted exposure map, and the un-vignetted exposure map. The former represents the cosmic X-ray background with an astrophysical origin, while the latter represents the intrinsic instrumental noise. ESPLINEMAP then finds the best-fit linear combination of the two templates and generates the background map. The details of this method are described in Cappelluti et al. (2007). The background maps are used for the PSF-fitting based source detection task described in Step (iv).
- (iii) We run EWAVELET again for each observation. This time the source list is generated by running EWAVELET on the exposure map and image coadded across the PN, MOS1, and MOS2 exposures (when available) with the default likelihood threshold (THRESHOLD=5).
- (iv) For each EWAVELET source list, we use the SAS task EMLDETECT to re-assess the detection likelihood and determine the best-fit X-ray positions. EMLDETECT is a PSF-fitting tool, which performs maximum-likelihood fits to the input source considering the *XMM-Newton* PSF, exposure values, and background levels of the input source on each image. EMLDETECT also convolves the PSF with a β -model brightness profile for clusters and uses the result to determine if the input source is extended. We use a stringent likelihood threshold (LIKMIN= 10.8) to ensure that astrometric corrections are calculated based on real detections.
- (v) For the mosaic-mode observations, the multiple pointings under the same ObsID were already registered on the same WCS frame. Therefore, we do not correct the astrometry for each pseudo-exposure but only consider the astrometric offsets on an ObsID-by-ObsID basis. The source lists for the mosaic-mode observations were generated using the SAS task EMOSAIC_PROC, which is a mosaic-mode wrapper for procedures similar to (i)–(iv) described above.

For steps (iv) and (v), the source searching was conducted simultaneously on the images of the three EPIC-cameras as the astrometric offsets between PN, MOS1, and MOS2 are negligible. For each ObsID, we cross-correlate the high-confidence EMLDETECT list of point sources (with the EMLDETECT flag EXT= 0) with the optical source catalog culled from the Subaru Hyper Suprime Cam Survey Public Data Release 1 (HSC-PDR1; Aihara et al. 2017), which is an ultra-deep optical photometric catalog with sub-arcsec angular resolution. The astrometry of HSC-PDR1 is calibrated to the PAN-STARRS1 3π survey and has a $< 0.05''$ astrometric uncertainty. More details of the HSC-PDR1 catalog can be found in Aihara et al. (2017), and it is also briefly discussed in §5. For astrometric corrections, we limit the optical catalog to HSC sources with $23 < i < 18$ to minimize possible spurious matches and matches to bright stars that might have proper motions or parallaxes. The offset between each ObsID and the HSC catalog is calculated

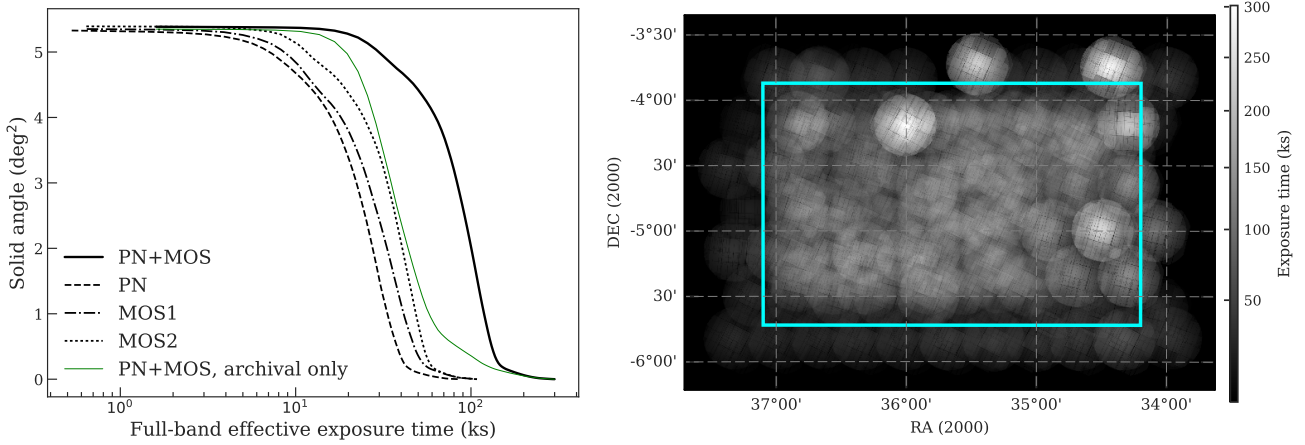


Figure 2. *Left* – Cumulative survey solid angle as a function of full-band effective exposure for observations used in this work. *Right* – Full-band survey exposure map (PN + MOS), the 5.3 deg^2 survey region from which the X-ray source catalog is constructed is marked as the rectangular box. Except for several regions with deep *XMM-Newton* follow-up observations of galaxy clusters, the *XMM-Newton* coverage in our source-extraction region is generally homogeneous.

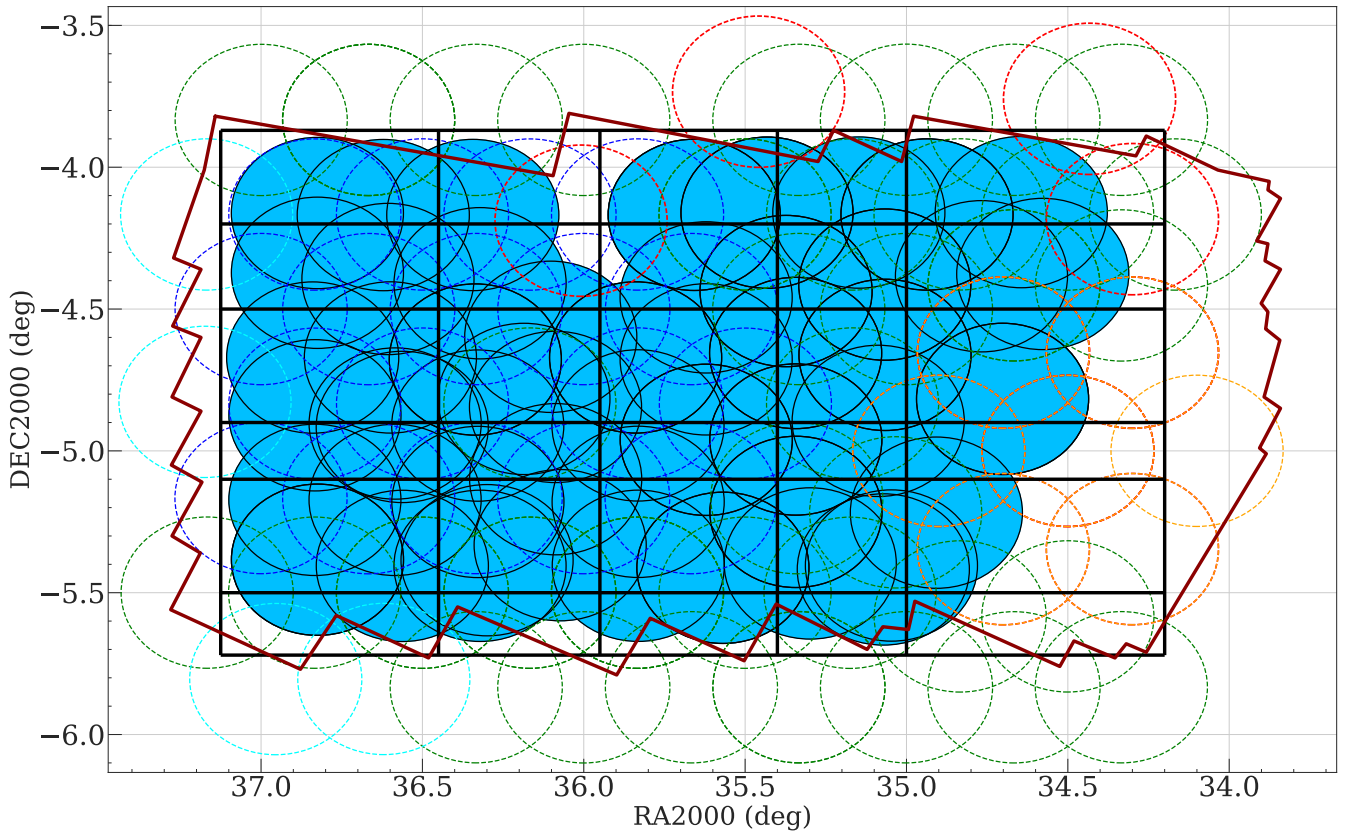


Figure 3. Locations of the *XMM-Newton* observations used in this work. The AO-15 observations are marked as the blue-filled circles with solid boundaries. The archival observations are marked as dashed circles. Circles with green, orange, blue, and cyan colors are for XMM-LSS, SXDS, XMDS, and XMM-XXL observations, respectively. We also show the detection grid used for running EMLDETECT. In each cell of the grid, all of the observations with non-zero exposure time in the cell are considered for source detection, and only the sources with coordinates inside the cell are kept. The final source catalog is the union of the source lists from all cells. We also plot the RA/DEC range of our catalog selection area as the solid rectangle, and the *Spitzer* SERVS footprint is marked as the red polygon. Note that our AO-15 observations do not cover the entirety of the source-extraction region, because the existing data from SXDS (bottom-right corner) and from deep X-ray cluster follow-up observations (top-middle and top-right, the red circles) are already at the desired depth.

based on a maximum likelihood algorithm similar to the SAS task EPOSCORR. The major difference between our approach and EPOSCORR is that we use an iterative optimization approach compared to the grid-searching algorithm adopted by EPOSCORR. During each iteration, we cross-correlate the optical catalog with the X-ray catalog using a $3''$ search radius and exclude all duplicated matches (typically only $< 5\%$ of the X-ray sources have more than one optical counterparts in the bright HSC-PDR1 catalog). We then calculate the required corrections that maximizes the cross-correlation likelihood. After each iteration, we apply the best-fit astrometric offsets onto the source list and next repeat the catalog cross-correlation steps and re-calculate the required corrections using the updated coordinates of the source list. The required corrections usually converges after 1–2 iterations. For the purpose of frame-correction, we adopt the X-ray positional uncertainties calculated based on the PSF-fitting likelihood ratios provided by EMLDETECT (σ_{eml} hereafter). To avoid over-weighting sources with extremely small σ_{eml} , we also include an irreducible systematic uncertainty when finding the best-fit values for frame-correction.⁵ The median number of X-ray sources sources in an ObsID with only one HSC counterpart within $3''$ is 32.

The required frame-correction offsets calculated using our approach are less than $3''$ in both RA and DEC directions and are generally consistent with the results calculated using EPOSCORR, with a median difference of $0.1''$. For several obsIDs the difference between our offsets and the EPOSCORR offsets are non-negligible ($> 0.5''$). We visually inspect these ObsIDs and find that our approach does improve the alignments between the optical and corrected X-ray images. The event files and the attitude file for each ObsID are then projected onto the common WCS frame of the HSC catalog by updating the relevant keywords using a modified version of ALIGN-EVT (Ranalli et al. 2013). Since the sky coordinates for the event files of the mosaic-mode pseudo-pointings are derived based on the reference point centered at the nominal RA and DEC positions of the mosaic-mode ObsIDs, we also recalculate the sky coordinates for these event files with the SAS task ATTCALC using the true pointing positions as the reference point, which is necessary for using regular SAS tasks for mosaic-mode pseudo-exposures.

3.2 Second-pass source detection

We re-create images, exposure maps, detector masks, background maps using the frame-corrected event files and attitude files. We then run source detection tasks for the second time considering all *XMM-Newton* observations listed in Table 1. Similar to the approach used for the XMM-H-ATLAS survey (Ranalli et al. 2015), we divide the XMM-LSS field into a grid when running the second-pass source detection (see Fig. 3). We then use a custom-built wrapper of relevant SAS tasks to carry out the second-pass source detection, which is similar to the GRIDDETECT⁶ tool built for the XMM-H-ATLAS survey (Ranalli et al. 2015).

⁵ We assume the systematic uncertainties to be $0.5''$ as suggested by Watson et al. (2008).

⁶ <https://github.com/piero-ranalli/griddetect>.

For each cell in the grid, we co-add the images and exposure maps for all observations with footprint inside the cell and run EWAVELET with a low detection threshold⁷ on the co-added image and exposure map. For each cell, we only keep EWAVELET sources within the RA/DEC range of the grid (with a $1'$ padding on each side of the cell). The cell sizes are determined by the number of EWAVELET sources and the number of ObsIDs encompassed because the number of images that can be processed by a single EMLDETECT thread is limited. We then use the EWAVELET list as an input for EMLDETECT to assess the detection likelihood. Instead of running on the co-added image, EMLDETECT takes the image, exposure map, background map, and detector mask of each input observation into account. The EMLDETECT point-source list of the full XMM-LSS region is constructed from the union of the sources from all cells after removing duplicates due to the “padding”. We search for sources in three different bands: 0.5–2 keV (soft), 2–10 keV (hard), and 0.5–10 keV (full). We consider sources with EMLDETECT likelihood larger than DET_ML = 6.0 to be reliably detected. This corresponds to a false-detection probability of 2.5×10^{-3} . A total of 5218 sources satisfy this criterion in at least one of the three bands. For readers interested in an even more reliable catalog, we suggest using the DET_ML = 10.8 detection threshold (equivalent to a false-detection probability of 2×10^{-5}) for the final X-ray catalog. A total of 4854 sources have DET_ML ≥ 10.8 in at least one bands. The detection thresholds are determined by extensive simulations that are discussed in §4. We show the spatial distribution of the 5218 detected sources Fig. 4.

3.3 Astrometric accuracy

We investigate the positional accuracy of the *XMM-Newton* sources by comparing the second-pass X-ray catalog with the HSC-PDR1 catalog. Similar to the frame-correction procedures described in §3.1, we search for unique optical counterparts around the X-ray positions using a $3''$ search radius. For the 5136 X-ray sources detected in the full-band during the second-pass source-searching process, a total of 2085 X-ray sources are found to have only one $i = 18 - 23$ HSC counterpart within $3''$. We use the separations between the optical and X-ray positions of this subsample as a means to determine empirical X-ray positional uncertainties, which is a commonly adopted practice in deep X-ray surveys (e.g. Luo et al. 2010; Xue et al. 2011; Luo et al. 2017).

The X-ray positional accuracy is determined by how well the PSF-centroid location can be measured, which usually depends on the number of counts of the detected source and the PSF size of the instrument. For the vast majority of the X-ray sources presented in this work, the detected photons come from at least three different observations. Therefore, the dynamical range of off-axis angle for our sources is relatively small, and thus the PSF size (i.e. off-axis angle) dependence to positional uncertainty is weak. On the other hand, the X-ray positional uncertainty is strongly dependent on the number of counts available for detected sources. Using the angular separation between the 2085 X-ray sources

⁷ THRESHOLD=4.

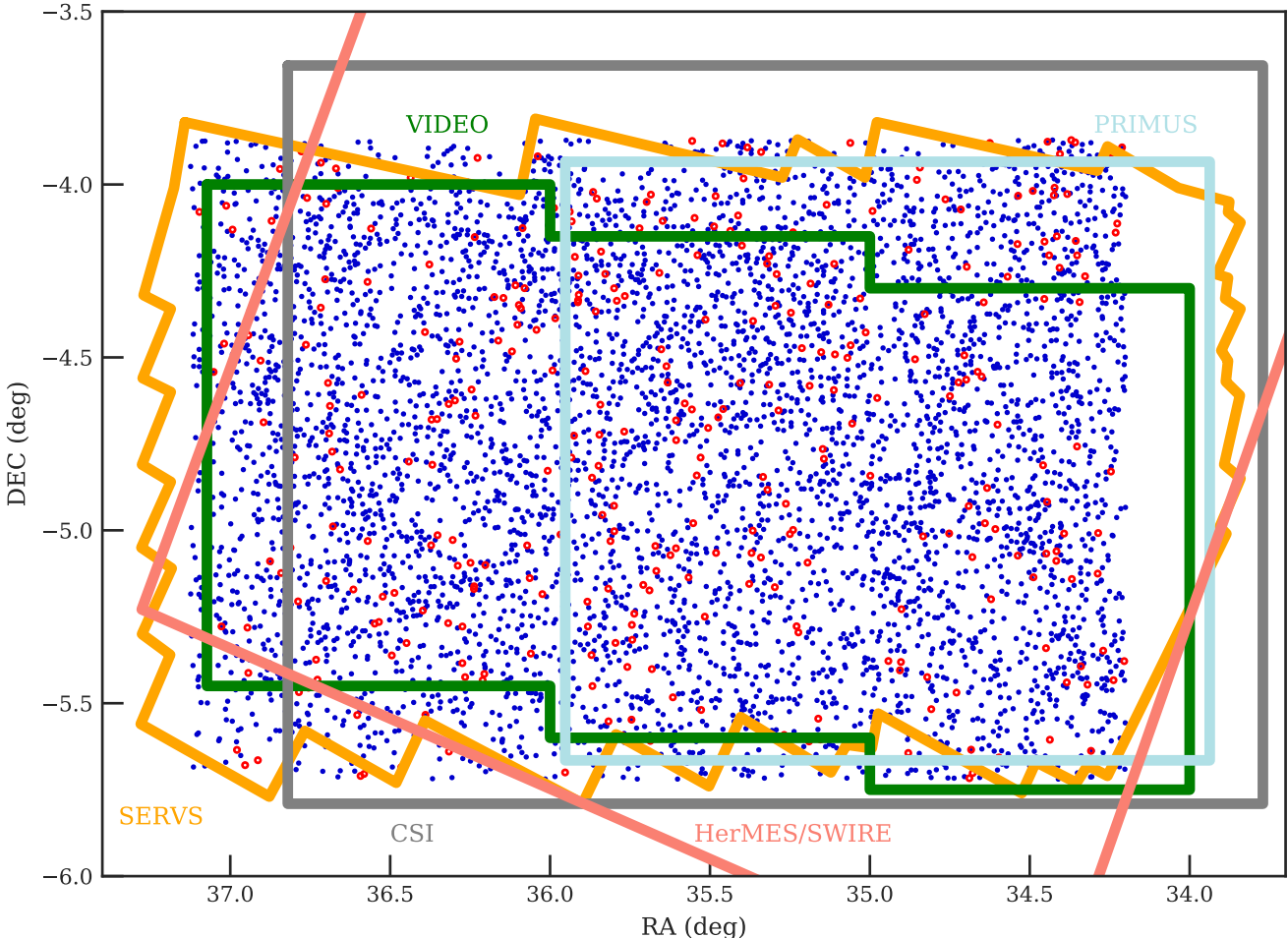


Figure 4. Spatial distribution of the 5218 sources detected in this work. We have identified reliable multiwavelength counterparts (see Sec. 5.1 and Sec. 5.2 for details) for 97% of the *XMM-Newton* sources (blue dots), while the remaining 3% of sources are marked as open circles. Some of the excellent multiwavelength coverage of the XMM-LSS field (see Table 1) is also shown as labeled.

and their unique optical counterparts, we derive an empirical relation between the number of X-ray counts, C ,⁸ and the 68% positional uncertainty radius ($r_{68\%}$) for the full-band-detected X-ray sources, $\log_{10} r_{68\%} = -0.31 \times \log_{10} C + 0.85$. The parameters are chosen such that 68% of the sources have positional offsets smaller than the empirical relation.

The X-ray positional uncertainty, σ_x , is $r_{68\%}$ divided by a factor of 1.51517 (e.g., Pineau et al. 2017). Because the separations in both RA and DEC behave as a univariate normal distribution with σ_{RA} and σ_{DEC} , respectively,⁹ the angular separation should therefore follow the joint probability distribution function of the uncertainties in the RA and DEC directions. Considering the case where $\sigma_{RA} = \sigma_{DEC}$, the angular separation between an optical source and an X-ray source should follow the univariate Rayleigh distribution with the scaling parameter σ_x , where $\sigma_x = \sigma_{RA} = \sigma_{DEC}$ (see §4

⁸ An upper limit of 2000 is set on C because the improvement of positional accuracy is not significant for larger source counts (e.g., Luo et al. 2017).

⁹ Here we consider the positional uncertainties of the HSC-PDR1 catalog to be negligible compared to the *XMM-Newton* positional uncertainties.

of Pineau et al. 2017, for details). Since σ_x is not the standard deviation of a 2D normal distribution, the 68% uncertainty of the angular separation is represented as $r_{68\%} = 1.51517\sigma_x$. The factor 1.51517 is determined by integrating the Rayleigh distribution until the cumulative probability reaches 0.68. For reference, 90%, 95%, and 99.73% uncertainties corresponds to $2.3\sigma_x$, $2.7\sigma_x$, $4.3\sigma_x$, respectively.

For each energy band, we repeat the same process to find the best-fit relation for σ_x using the following equation:

$$\log_{10} \sigma_x = \alpha \times \log_{10} C + \beta. \quad (1)$$

Due to the large PSF size of *XMM-Newton*, it is possible that the positional uncertainties were underestimated when deriving Equation 1 using only the optical sources within the 3'' search radius. Therefore, we adopt an iterative process. For each iteration, we use the derived σ_x to find reliable matches using the likelihood-ratio matching method described in §5.1. We then re-derive Equation 1 using the reliable matches, and the updated astrometric uncertainties are used for running likelihood-ratio matching again. This is a stable process, as the parameters converge after 2–3 iterations. The average positional uncertainties (σ_x) for

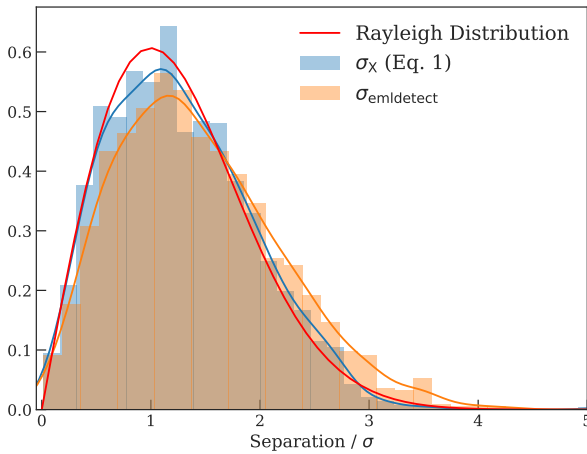


Figure 5. Histograms of the “normalized positional offsets” and comparison with the expected Rayleigh distribution, the solid red curve. The distribution for the positional offsets normalized by the empirically derived positional uncertainty, σ_x , for the sources matched to bright optical counterparts is marked as the blue histogram along with the kernel density estimation. The distributions of the positional offsets normalized by the EMLDETECT-derived positional uncertainties, σ_{eml} , are also shown.

our soft-band, hard-band, and full-band X-ray catalogs are $1.35''$, $1.37''$, and $1.31''$, respectively. In Fig. 5, we show a comparison of the normalized separation ($\text{Separation}/\sigma$) between the full-band X-ray sources and their bright optical counterparts with σ derived using Eq. 1, σ_x , and the original positional uncertainties calculated by EMLDETECT, σ_{eml} . The agreement between the Rayleigh distribution and the $\text{Separation}/\sigma_x$ distribution of our sample demonstrates that our empirically derived σ_x are reliable indicators of the true positional uncertainties. As for σ_{eml} , previous studies have identified that an irreducible systematic uncertainty should be added to σ_{eml} for the normalized separation to follow a Rayleigh distribution (e.g., Watson et al. 2008), but the nature of this systematic uncertainty remains unclear. We use σ_x as the positional uncertainties of our X-ray catalog, but σ_{eml} is also included in the final catalog for completeness.

3.4 The main X-ray source catalog

We detect 5136, 3878, 2655 point sources with $\text{DET_ML} > 6.0$ in the $0.5\text{--}10$ keV, $0.5\text{--}2$ keV, and $2\text{--}10$ keV bands, respectively. We report the details of the main X-ray source catalog in Table 7 of Appendix A. The extended sources (identified by the $\text{EXT} > 0$ flag of EMLDETECT) are not included as the properties of the extended X-ray emission are beyond the scope of this work.¹⁰ We associate catalogs from the three energy bands using a similar approach to that adopted by the *XMM-Newton* Serendipitous Source Catalogue. We consider two sources from different catalogs to be the same if their angular separation is smaller than any of the following quantities: (1) $10''$ (2) distance to the nearest-neighbor in

¹⁰ There are 68, 77, 11 sources identified as $\text{EXT} > 0$ by EMLDETECT at the $0.5\text{--}10$ keV, $0.5\text{--}2$ keV, and $2\text{--}10$ keV bands, respectively.

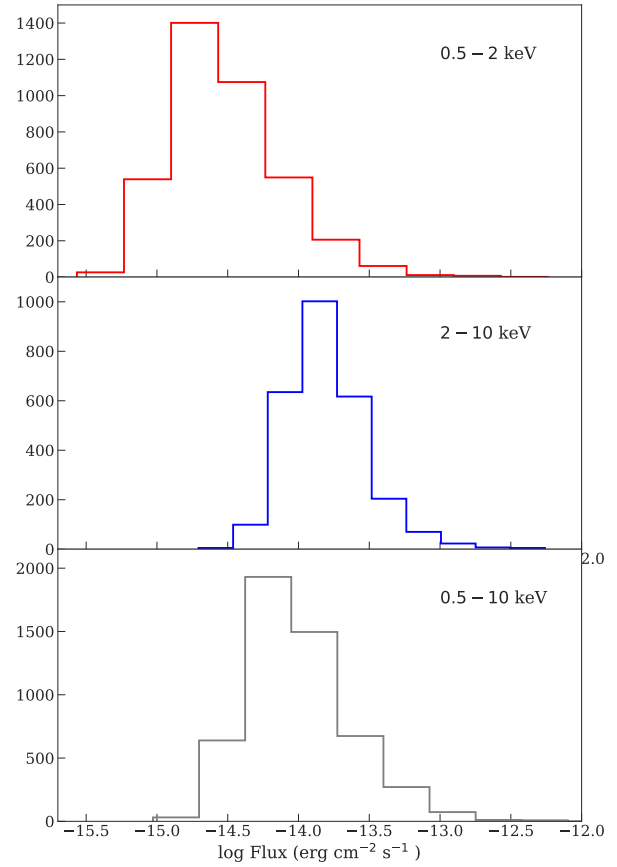


Figure 6. Flux distributions of the sources detected in the soft (top panel), hard bands (middle panel), and full (bottom panel).

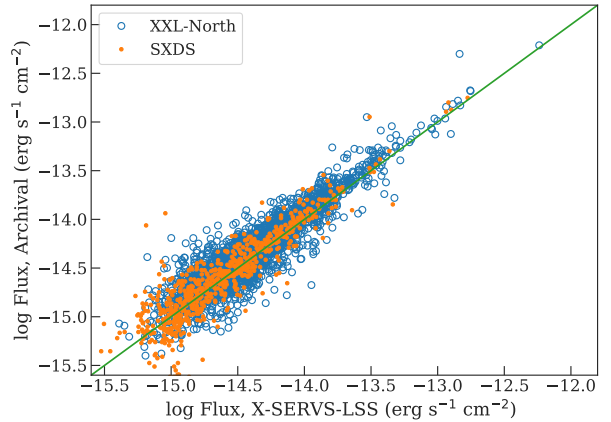


Figure 7. Comparison of the soft-band X-ray fluxes of our X-ray sources and those of the *XMM-Newton* counterparts identified in the archival source catalogs within a $10''$ radius, including XXL-North (blue open circles) and SXDS (orange dots).

each catalog (3) Quadratic sum of the 99% positional uncertainties of both sources. The final source catalog is the union of the sources detected in the three energy bands. We check for potential duplicated sources by visually inspecting all sources with distance to the nearest-neighbor (DIST_NN) less than $10''$, and only one set of sources is found to be duplicated, resulting in a total of 5218 unique sources. A unique

X-ray source ID is assigned to each of the 5218 sources at this stage.

We also derive the count-rate to flux energy conversion factors (ECFs) assuming a power-law spectrum with photon index $\Gamma = 1.7$, which is typical for X-ray AGNs (e.g., Ranalli et al. 2015), and Galactic absorption, $N_{\text{H}} = 3.57 \times 10^{20} \text{ cm}^{-2}$.¹¹ The conversion factors for PN and MOS are (7.06, 1.99), (1.24, 0.44), and (3.17, 0.96) counts $\text{s}^{-1}/10^{-11}\text{erg cm}^{-2} \text{ s}^{-1}$, in the 0.5–2 keV, 2–10 keV, and 0.5–10 keV bands, respectively. For each source detected by EMLDETECT, the flux from each EPIC camera is calculated separately using the corresponding ECF. The final flux of the source is the error-weighted mean of the fluxes from the three EPIC cameras, when available. We show the flux distributions of the sources detected in the three energy bands in Fig. 6.

For sources that are not detected in all three bands, we calculate the source-count upper limits using the mosaicked background map of the band in which the source is not detected. The mosaicked background map of each band is generated by summing the background maps from all individual observations. According to the Poisson probability set by the EMLDETECT detection likelihood threshold (P_{Random} , the probability of the detected source being a random Poisson fluctuation due to the background), we can calculate the minimum required source counts (m in the following equation) to exceed the random background fluctuations, B , using the regularized upper incomplete Γ function:

$$P_{\text{Random}} = \frac{1}{\Gamma(m)} \int_B^\infty t^{m-1} e^{-t} dt \quad (2)$$

Note that $\Gamma(m)$ is the Γ function, which is equivalent to $(m-1)!$. The upper limits are set at $P_{\text{Random}} = 2.5 \times 10^{-3}$ (consistent with $\text{DET_ML} = 6$). For each non-detected source in each band, we determine the background counts by summing up the background map within the circle with 70% energy encircled fraction (EEF). We then calculate m using the SCIPY function SCIPY.SPECIAL.GAMMAINCCINV.¹² The flux upper limit is calculated based on the following equation:

$$S = \frac{m - B}{\exp \times \text{EEF} \times \text{ECF}} \quad (3)$$

Here $\text{EEF} = 0.7$, and \exp is the median exposure time within the 70% EEF circle. The upper limits of the source count and source count rate are also corrected for PSF loss. The flux upper limits are calculated as the exposure-time-weighed mean of the three EPIC detectors.

For each source detected in either the soft or the hard band (or both), we calculate its hardness ratios (HR) defined as $(H-S)/(H+S)$, where H and S are the source counts weighted by the vignetting-corrected exposure times in the hard and the soft bands, respectively. Note that the source counts here are the default output of EMLDETECT, which is the sum of the counts from all three EPIC detectors. We report this value in our catalog for direct comparison with

¹¹ Derived using the COLDEN task included in the CIAO software package. The Galactic column density is calculated at the center of the source-detection region at RA=35.6625°, DEC=−4.795°.

¹² This is the inverse function of Equation 2.

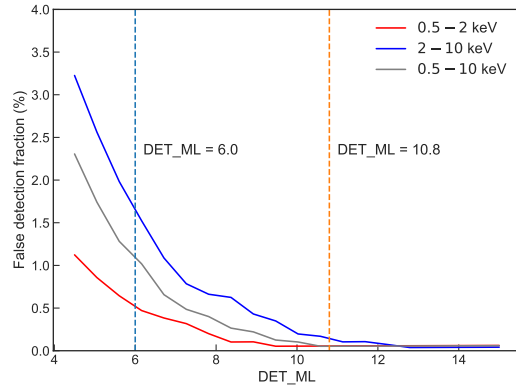


Figure 8. The fraction of spurious sources detected at different DET_ML based on simulations. The detection thresholds relevant to our catalog are marked as the dashed lines.

previous studies. The uncertainties on HR are calculated based on the count uncertainties from the output of EMLDETECT using the error propagation method described in §1.7.3 of Lyons (1991).

As a comparison, we also match our X-ray catalog with two archival *XMM-Newton* catalogs in the XMM-LSS region, the XXL-North catalog (Liu et al. 2016) and the Subaru X-ray Deep Field catalog (Ueda et al. 2008). We match these catalogs to our X-ray sources by searching for counterparts within a 10'' radius. A total of 2843 X-ray sources from XXL-North and 714 from SXDS are found to have a counterpart within the 10'' radius in our X-ray catalog. For these matched sources, we show the comparison between the soft-band X-ray fluxes reported in these archival catalogs and those in our catalog in Fig. 7. As expected, the majority of the archival sources detected in our catalog have consistent soft-band fluxes. Since the SXDS observations were also used for constructing the XXL-North (Liu et al. 2016) catalog, we conclude that at we have detected 2375 new X-ray sources in our survey.

4 SURVEY SENSITIVITY AND $\log N - \log S$

4.1 Monte Carlo simulation

To assess our survey sensitivity, we perform Monte Carlo simulations of mock X-ray observations. For each simulation, we generate a list of mock X-ray sources by sampling from the $\log N - \log S$ relations reported in the XMM-COSMOS survey (Cappelluti et al. 2009, for the 0.5–2 keV and 2–10 keV bands) and the Chandra Multiwavelength Project survey (ChaMP, Kim et al. 2007, for the 0.5–10 keV band). The maximum flux of the mock X-ray catalogs is set at $10^{-11} \text{ erg cm}^{-2} \text{ s}^{-1}$. The minimum flux of the mock X-ray sources at each energy band is set as 0.5 dex lower than the minimum detected flux (e.g. LaMassa et al. 2016). We randomly place the mock X-ray sources in the RA/DEC range covered by the *XMM-Newton* observations used in this work. We then use a modified version of the simulator written for the *XMM-Newton* survey of the CDF-S (Ranalli et al. 2013),

CDFS-SIM,¹³ to create mock event files. CDFS-SIM converts X-ray fluxes to PN and MOS count rates with the same model used for deriving the ECFs, and it then randomly places X-ray events around the source location according to the count rates, the *XMM-Newton* PSFs at the given off-axis angle, and the real exposure maps. We extract images from the simulated event files using the same methods described in §3. For each observation, the simulated image is then combined with a simulated background, which is created by resampling the original background map according to Poisson distributions to create simulated images that mimic the real observations. For each energy band, a total of 20 simulations are created.

We run the same two-stage source-detection procedures described in §3 on the simulated data products. For each simulation, we match the detected sources to the input sources within a 10'' search radius by minimizing the quantity R^2 :

$$R^2 = \left(\frac{\Delta\text{RA}}{\sigma_{\text{RA}}} \right)^2 + \left(\frac{\Delta\text{DEC}}{\sigma_{\text{DEC}}} \right)^2 + \left(\frac{\Delta\text{RATE}}{\sigma_{\text{RATE}}} \right)^2 \quad (4)$$

This takes into account the flux and positional differences between the input catalog and the sources detected in the simulated images (e.g., Cappelluti et al. 2007; Ranalli et al. 2015). For detected sources without any input sources within the 10'' radius, we consider them to be spurious detections. In Fig. 6, we show the spurious fraction as a function of DET_ML for the soft, hard, and full bands. For our catalog, we consider sources with DET_ML > 6 to be reliably detected. At this threshold, the spurious fractions are 0.73%, 2.01%, and 1.68% for the soft, hard, and full bands, respectively. As for the threshold at DET_ML = 10.8, the spurious fractions become 0.08%, 0.34%, and 0.10%, respectively. The low spurious fraction in the soft-band is likely due to its lower background level. For the full X-ray source catalog of 5218 sources, these spurious fractions translate to ≈ 41 spurious detections for DET_ML > 6, and 12 spurious detections for DET_ML > 10.8.

4.2 Survey sensitivity, sky coverage, and $\log N - \log S$

We create sensitivity maps of our survey region in different bands using the background maps and exposure maps generated as described in §2.2. The mosaicked background and exposure maps are binned to 5×5 pixels ($\approx 20'' \times 20''$). For each pixel on the binned, mosaicked background map, the minimum required source counts to exceed the random background fluctuation are calculated using Equation 2. The sensitivity is then calculated using Equation 3 with the corresponding EEF and ECF values. We show the sky coverage in Fig. 10, and the soft-band sensitivity map in Fig. 9.

We calculate the $\log N - \log S$ relations of our survey using the sky coverage curves described above and the following equation:

$$N(>S) = \sum_{i=1}^{N_s} \frac{1}{\Omega_i} \quad (\text{deg}^{-2}) \quad (5)$$

¹³ <https://github.com/piero-ranalli/cdfs-sim>

The $\log N - \log S$ relations of our survey are shown in Fig. 11, along with a selection of the relations from the literature. The flux differences caused by different choices of power-law indices and/or the slight difference in energy range have been corrected to those used in this work. Considering factors such as different spectral models and/or methods of generating survey sensitivity curves, our $\log N - \log S$ relations are consistent with the relations reported in the literature.

5 MULTIWAVELENGTH DATA IN THE XMM-LSS FIELD

The XMM-LSS region is one of the most extensively observed extragalactic fields. The publicly available multiwavelength observations in the XMM-LSS region utilized in this work are the *Spitzer* Extragalactic Representative Volume Survey (Mauduit et al. 2012), the *Spitzer* SWIRE survey (Lonsdale et al. 2003), the VISTA Deep Extragalactic Observations (VIDEO) survey (Jarvis et al. 2013), the CFHTLS-wide survey (Hudelot et al. 2012), and the Subaru HSC Survey Public Data Release 1(HSC-PDR1, Aihara et al. 2017).

We focus on finding the correct counterparts for our X-ray sources in four deep optical-to-near-IR (OIR) catalogs, SERVS, VIDEO, CFHTLS, and HSC-PDR1. SERVS is a post-cryogenic *Spitzer* IRAC survey in the near-IR 3.6 and 4.5 μm bands with $\approx 2\mu\text{Jy}$ survey sensitivity limits and ≈ 5 deg 2 solid angle coverage in the XMM-LSS region. We make use of the highly reliable two-band SERVS catalog built using SExtractor, obtained from the *Spitzer* Data Fusion website,¹⁴ which has $\approx 4 \times 10^5$ sources. 87% of the X-ray sources have at least one SERVS counterpart within their 99% positional-uncertainty radius ($r_{99\%}$ hereafter).

VIDEO is a deep survey in the near-infrared Z , Y , J , H and K_s bands with $\approx 80\%$ completeness at $K_s < 23.8$ and a total of $\approx 5.7 \times 10^5$ sources. 84% of the X-ray sources have at least one VIDEO counterpart within $r_{99\%}$.

The CFHTLS-W1 survey covers the entirety of our X-ray data, with an 80% completeness limit of $i' = 24.8$. We select the CFHTLS sources in the RA/DEC ranges marginally larger (1') than our source detection region. We limit the CFHTLS sources to those with $\text{SNR} > 5$ at i' -band. The total number of sources in the i' -band selected catalog is $\approx 8.1 \times 10^5$. 96% of the X-ray sources in our catalog have at least one CFHTLS counterpart within $r_{99\%}$. Although CFHTLS is not as deep as HSC-PDR1 at g , r , i , z bands, it has the complementary u^* -band photometry. Including photometry from CFHTLS also ensures that we will not miss an optical counterpart due to bad photometry caused by artifacts such as satellite tracks in one of the two surveys.

The XMM-LSS field is entirely encompassed by the 108 deg 2 HSC-PDR1-wide survey. Inside the XMM-LSS field, HSC-PDR1 also has “ultra-deep” (≈ 1.77 deg 2) and “deep” (≈ 5 deg 2) surveys, which overlap with the SXDS and XMDS regions, respectively. The limiting magnitudes in the i -band for the ultra-deep, deep, and wide HSC-PDR1 surveys are 27.2, 26.5, and 26.4, respectively. We select the i -band detected HSC-PDR1 sources in the RA/DEC

¹⁴ <http://www.mattiaaccari.net/df/>.

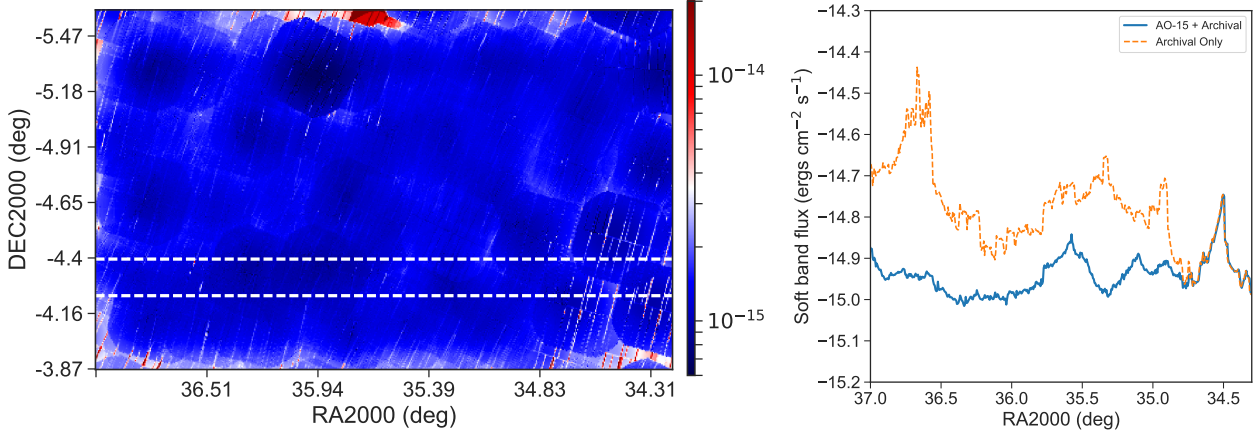


Figure 9. Left – Soft-band sensitivity map of the source-extraction region (the same as the cyan box shown in Fig. 2 and Fig 3). Right – Median sensitivity as a function of RA in the region marked between the two dashed lines of the left panel (solid line). For comparison, we also show the distribution of the sensitivity map generated using archival data only as the dashed line, which demonstrates the homogeneity of sensitivity across the wide field enabled by the new data.

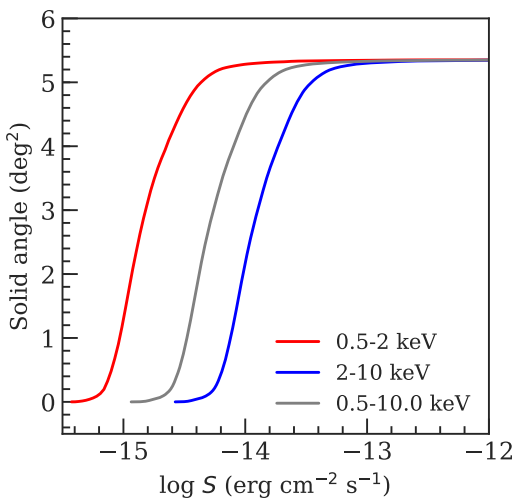


Figure 10. Sky coverage in the soft, hard, and full bands of our X-ray survey in XMM-LSS.

ranges slightly larger than our source detection region. The HSC-PDR1 sources used for our source-matching are the union of the ultra-deep, deep, and wide surveys with the DETECT_IS_PRIMARY and IDETECTED_NOTJUNK flags set as TRUE, and CENTROID_SDSS_FLAGS set as FALSE. According to the HSC-PDR1 example script for selecting “clean objects”, we also exclude the HSC sources with FLAGS_PIXEL_EDGE, FLAGS_PIXEL_SATURATED_CENTER, FLAGS_PIXEL_CR_CENTER, FLAGS_PIXEL_BAD flags in the *i*-band to avoid unreliable *i*-band sources. The HSC catalogs from the three different depth layers were merged according to their OBJECT_ID. To avoid duplications, sources from the HSC wide survey within $0.5''$ of any sources from either the deep or ultra-deep survey are discarded. Similarly, sources from the deep survey with distance less than $0.5''$ from any ultra-deep sources are also discarded. The total number of HSC-PDR1 sources in our source detection re-

gion is $\approx 3.2 \times 10^6$, and $\approx 96\%$ of the X-ray sources in our main catalog have at least one HSC-PDR1 counterpart $r_{99\%}$.

5.1 The likelihood ratio method

To match reliably the X-ray sources to the OIR catalogs with much higher source densities, we employ the maximum likelihood estimation method (MLE hereafter) similar to previous deep X-ray surveys, (e.g., Brusa et al. 2007; Luo et al. 2010, 2017). The likelihood ratio (*LR* hereafter) is defined as the ratio between the probability that the source is the correct counterpart, and the probability that the source is an unrelated background object (Sutherland & Saunders 1992):

$$LR = \frac{q(m)f(r)}{n(m)}. \quad (6)$$

Here $q(m)$ is the magnitude distribution of the expected counterparts, $f(r)$ is the probability distribution function of the angular separation between X-ray and OIR sources, and $n(m)$ is the magnitude distribution of the background sources.

We calculate the background source magnitude distributions using OIR sources between $10''$ and $50''$ from any sources in our X-ray catalog.

As discussed in §3.3, the probability distribution function of the angular separation should follow the Rayleigh distribution:

$$f(r) = \frac{r}{\sigma_x^2} \exp^{-\frac{r^2}{2\sigma_x^2}}. \quad (7)$$

Note that Equation 7 is different from the two-dimensional Gaussian distribution function that maximizes at $r=0$, and thus the *LR* values calculated in this work are not directly comparable to previous works that adopted a Gaussian $f(r)$.

The magnitude distribution of the expected counterparts, $q(m)$, is often approximated by taking all counterparts within a small search radius and then deriving $q(m)$ by subtracting the expected number of background sources within the search radius (e.g., Brusa et al. 2007; Marchesi et al.

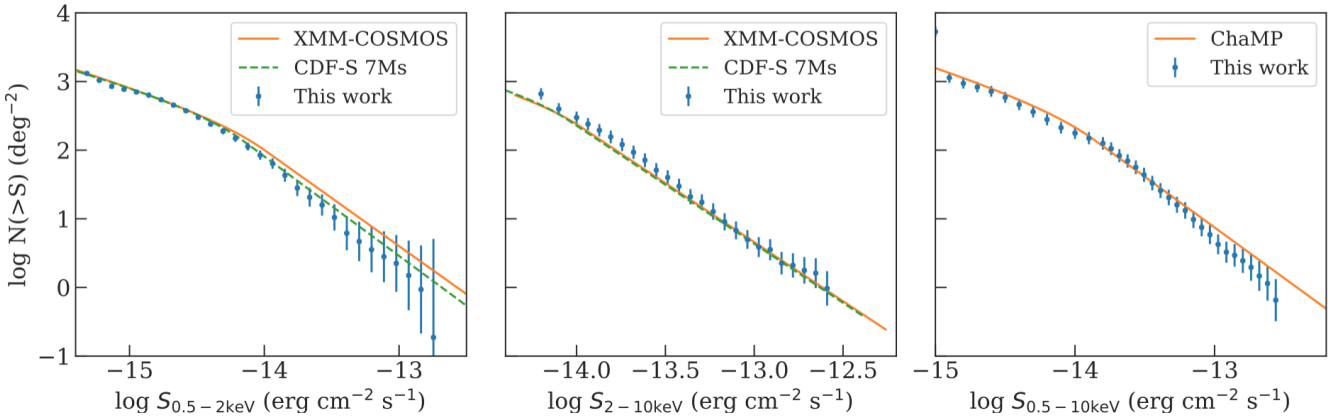


Figure 11. The $\log N - \log S$ relations for our catalog in the soft-band (left), hard-band (middle), and full-band (right). For comparison, we also show some $\log N - \log S$ relations from the literature with appropriate energy range and power-law index corrections. The $\log N - \log S$ relations of our survey are generally consistent with previous studies.

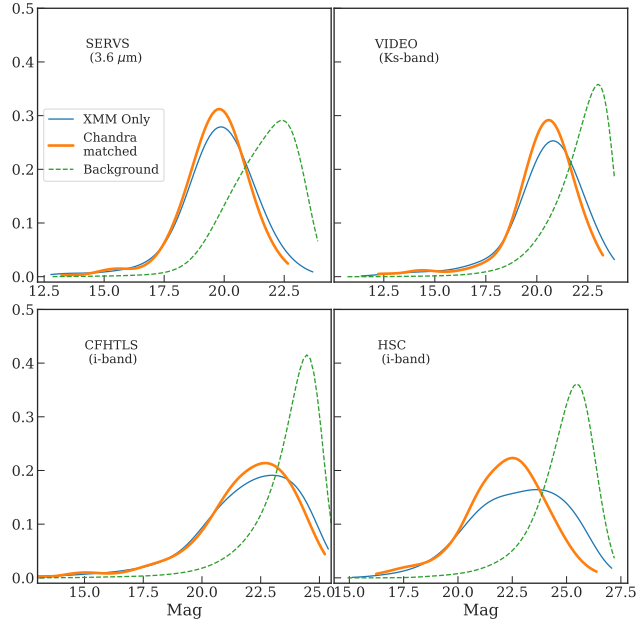


Figure 12. Kernel density estimations of the magnitude distributions (solid lines) for the expected counterparts in SERVS (top-left), VIDEO (top-right), CFHTLS (bottom-left), and HSC-PDR1 (bottom-right). We show the distributions obtained using the full *XMM-Newton* catalog ($q(m)_{XMM-Newton}$), and the distributions obtained using the *Chandra* sources in the XMM-LSS field ($q(m)_{Chandra}$). The magnitude distributions of the background, unrelated sources are also shown in each panel as the dashed curves. This figure demonstrates that $q(m)_{Chandra}$ significantly improves upon the background-dominated $q(m)_{XMM-Newton}$.

2016). Some studies also adopt an iterative approach to find $q(m)$ that optimizes the matching reliability and completeness (e.g., Luo et al. 2010). These approaches can be quite uncertain for our survey because of the larger positional uncertainties of *XMM-Newton* and the high source densities of the OIR catalogs, particularly for the deep optical surveys. Therefore, we obtain $q(m)$ for our X-ray sources by first matching our *XMM-Newton* catalog to the *Chandra*

Source Catalog 2.0 (CSC 2.0; Evans et al. 2010) to take advantage the higher angular resolution and positional accuracy of *Chandra*. We derive the positional uncertainties of the *Chandra* sources in our survey region using the same empirical approach described in Xue et al. (2011) by selecting CSC sources in the RA/DEC range of our catalog, and matching them onto HSC-PDR1 using a $1.5''$ radius. We select CSC sources that are uniquely matched to our X-ray catalogs within the 95% uncertainties (*Chandra* and *XMM-Newton* positional uncertainties are added in quadrature). A total of 241 *Chandra* sources are matched to our *XMM-Newton* catalog. We match these *Chandra* sources to the four OIR catalogs using Equation 6, with the $q(m)$ derived using the iterative approach described in Luo et al. (2010). The $q(m)$ derived from the CSC sources, $q(m)_{Chandra}$, is then used as an input for matching our *XMM-Newton* sources to OIR catalogs. We note that the X-ray flux distributions at soft, hard, and full bands of the *Chandra*-matched subsample are very similar to those of our entire *XMM-Newton* catalog, and therefore $q(m)_{Chandra}$ should be consistent with the intrinsic magnitude distributions of the real OIR counterparts of our full X-ray catalog. The counterpart matching processes are run on four different OIR catalogs: *Spitzer*-SERVS, VIDEO, CFHTLS, and HSC-PDR1. For illustration, we show the magnitude distributions of the background sources and those of the “reliable matches” derived using CSC sources in Fig. 12. For comparison, we also use the iterative method of Luo et al. (2010) to obtain $q(m)$ for the full *XMM-Newton* catalog, $q(m)_{XMM-Newton}$, using a $3''$ initial search radius, which is also plotted on Fig. 12. It is evident that for ultra-deep OIR catalogs such as HSC-PDR1, $q(m)_{XMM-Newton}$ would be skewed toward the faint background sources compared to the *Chandra*-matched subsample. For the other catalogs, we find no qualitative difference between $q(m)_{Chandra}$ and $q(m)_{XMM-Newton}$, but we still use $q(m)_{Chandra}$ for consistency.

We next compute the LR values for all OIR sources within a $10''$ radius of X-ray sources using Equation 6. For each OIR catalog, we choose the LR thresholds (LR_{th}) such that the reliability and completeness parameters are maximized (see Equation 5 of Luo et al. 2010 for details). Counterparts with $LR > LR_{th}$ are considered to be reliably

matched. The results are reported in Table 2. For each OIR catalog, we show the number of all X-ray sources with at least one OIR counterpart within the 99% positional uncertainties of the X-ray sources, N_{All} , and the number of X-ray sources with at least one reliably matched source with $LR > LR_{\text{th}}$, N_{Reliable} . For an X-ray source with only one OIR counterpart within the search radius but where its matching LR is smaller than LR_{th} , we consider the counterpart to be an acceptable match if the separation from the OIR position to the X-ray position is less than $r_{99\%}$. The total number of such cases for each OIR catalog is listed as $N_{\text{Acceptable}}$ in Table 2.

Motivated by the spurious matching rates (see §5.2 for the cross-matching reliability analysis), we first select a “primary” counterpart for each X-ray source from, in priority order of, SERVS, VIDEO, CFHTLS, and HSC-PDR1.¹⁵ After selecting the primary OIR counterpart, we then associate different OIR catalogs with each other using a simple nearest-neighbor algorithm. Thanks to the much smaller positional uncertainties of the OIR catalogs, we adopt a homogeneous search radius of $1''$ for the OIR catalog associations, which is the approach used by the *Spitzer* Data Fusion database (Vaccari 2016).

As a result, 4854 ($\approx 93\%$) X-ray sources have at least one reliable match. Of these sources, 3898 are matched to SERVS, 371 are matched to VIDEO, 382 are from CFHTLS, and 174 are from HSC. There are also 959 sources with multiple counterparts having $LR > LR_{\text{th}}$ in various OIR catalogs. For these sources, we select a “secondary” counterpart based on the strategies described below. First, if there are more than one reliable counterpart from SERVS or VIDEO, we select these second-best matches as the secondary counterpart. We find 62 secondary counterparts from SERVS and 29 from VIDEO. If the reliable counterparts with the maximum LR from HSC and CFHTLS are still not matched to any of the primary and secondary counterparts identified so far, we choose the secondary matches as the highest- LR CFHTLS counterparts (a total of 458 sources), then the highest- LR HSC counterparts (a total of 255 sources). There is also a small number of cases where the highest- LR counterparts from HSC and CFHTLS coincide with the SERVS/VIDEO primary counterparts, but still have a different counterpart with $LR > LR_{\text{th}}$ in CFHTLS or HSC. We then select these OIR sources as the secondary counterparts, where 96 of them are from CFHTLS and 100 of them are from HSC. Finally, there are 22 X-ray sources with three reliable counterparts; all of the tertiary counterparts are from CFHTLS (6) and HSC (16), which are also reported in our final catalog.

For the remaining X-ray sources without any of the counterparts with $LR > LR_{\text{th}}$, 61 ($\approx 1\%$) of them are considered to have “acceptable” matches, where 48, 7, and 6 of them are matched to SERVS, VIDEO, and CFHTLS, respectively. For the remaining sources, the vast majority of them still have at least one OIR counterpart within the relevant 99% positional uncertainty circle; only 23 sources are completely isolated. Visual inspection of these sources shows that most of the 23 sources coincide with a bright star, thus

¹⁵ Note that 85%, 10%, 1%, and 4% of the *Chandra* sources have their “primary” counterparts from SERVS, VIDEO, CFHTLS, and HSC-PDR1, respectively.

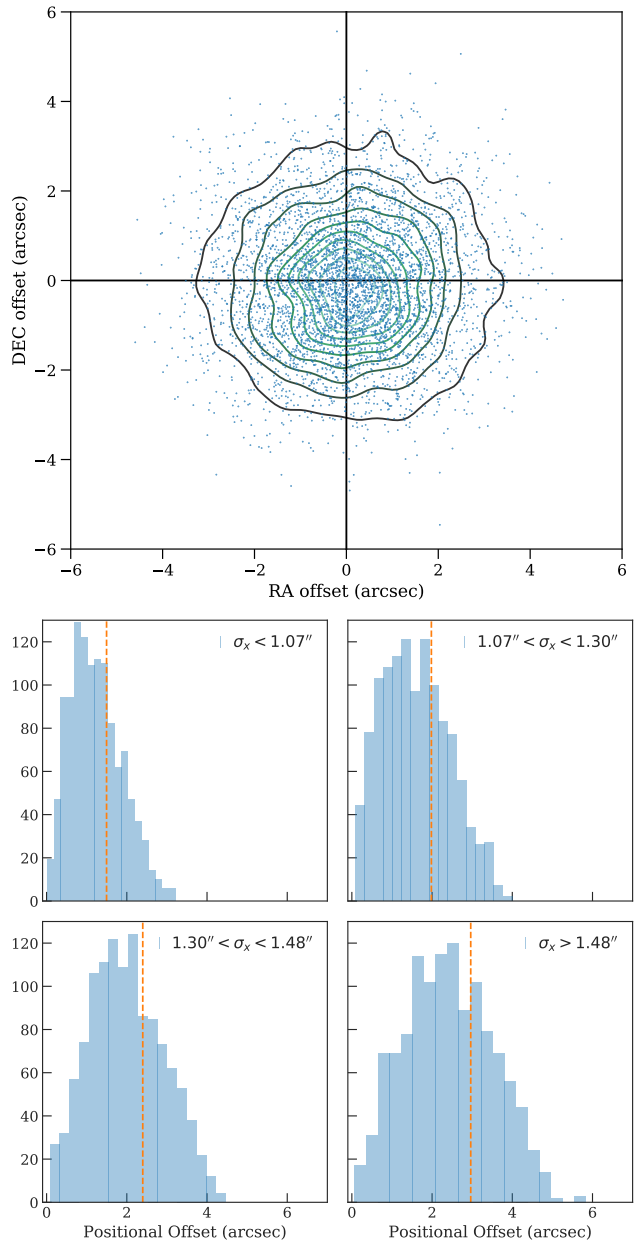


Figure 13. Top: Distribution of the positional offsets in the RA vs. DEC plane for the 4854 reliably matched sources. Note that the residual positional uncertainties are $< 0.1''$ in both the RA and DEC directions. Bottom: Histograms of positional offsets for the 4854 reliably matched sources, divided into four bins based on their positional uncertainties. In each panel, we also mark the 68% positional offset value as the dashed line.

making the pipeline OIR photometry unreliable. We plot the positional offsets between the X-ray sources and the reliably matched sources in Fig. 13.

5.2 Counterpart identification reliability

We assess the reliability of the MLE matching results using the Monte Carlo simulation approach described in Broos et al. (2007) and Xue et al. (2011). We consider our X-ray

Table 2. MLE counterpart matching results. Column 1: Catalog name. Column 2: Survey limits for each catalog in AB. Column 3: Survey area. Column 4: Positional uncertainty. Column 5: LR threshold. Column 6: Total number of X-ray sources with at least one counterpart within the 99% positional uncertainty in a catalog. Column 7: Average number of OIR sources within the 99% positional uncertainty radius of the X-ray sources. Column 8: Total number of X-ray sources with at least one counterpart with $LR > LR_{\text{th}}$. Column 9: Total number of X-ray sources without any reliable counterparts, but having only one counterpart within the 99% positional uncertainty of the X-ray source. Columns 10–12: See §5.2 for details. Column 10: The fraction of X-ray sources in the “associated population” based on the results of Monte Carlo simulations. Column 11: False matching rates determined using Monte Carlo simulations. Column 12: False matching rates determined based on comparing the matching results of the 241 *XMM-Newton* sources that also have archival *Chandra* detections, i.e., the fraction of these 241 X-ray sources to have different *XMM-Newton* matching results than the *Chandra* results.

Catalog	Limiting Magnitude	Area deg 2	σ	LR_{th}	N_{All}	$\bar{N}_{99\%}$	N_{Reliable}	$N_{\text{Acceptable}}$	f_{AP}	False Rate (Simulation)	False Rate (<i>Chandra</i>)
(1)	(2)	(3)	(4)	(5)	(6)	(7)	(8)	(9)	(10)	(11)	(12)
SERVS	$3.6\mu\text{m} < 23.1$	5.0	0.5''	0.34	4530	1.46	3898	259	96.8%	4.2%	2.7%
VIDEO	$K_s < 23.8$	4.5	0.3''	0.24	4285	1.88	3804	90	86.3%	8.0%	3.1%
CFHTLS-wide	$i < 24.8$	5.4	0.2''	0.27	5022	2.37	4138	129	75.6%	15.6%	5.7%
HSC-PDR1	$i < 26.5$	5.4	0.1''	0.13	5002	4.39	4192	52	78.6%	18.4%	6.4%
Summary	N/A	N/A	N/A	N/A	5218	N/A	4854	64	N/A		

sources consist of two different intrinsic populations, the “associated population” and the “isolated population”. The associated population is comprised of X-ray sources that do have a real counterpart in the corresponding OIR catalog, and the X-ray sources that should not have any OIR counterparts belong to the isolated population. For the associated population, counterpart-matching procedures can produce three different outcomes: (1) an X-ray source is matched to its correct counterpart (correct match, or CM), (2) an X-ray source is matched to an incorrect counterpart (incorrect match, or IM), and (3) no counterparts were recovered (false negative, or FN). For the isolated population, there are two possible matching results: (1) no counterparts are found (true negative, or TN), and (2) an OIR source is identified as a counterpart (false positive, or FP).

In order to estimate the fractions of X-ray sources in both populations for our catalog, we simulate each population separately. The details of the simulation setup can be found in the appendix of Broos et al. (2007) and §5 of Broos et al. (2011). We briefly summarize the simulation procedures as the following. (1) For the “associated population”, we remove all OIR sources considered to be a match in §5.1, then randomly shuffle the OIR catalogs, and then create mock OIR counterparts for each X-ray source in our catalog based on the X-ray and OIR positional uncertainties. (2) For the “isolated population”, we create mock X-ray sources that are at least 20'' away from any real X-ray sources. A total of 100 simulations are carried out for each population, and we run the MLE matching procedures on each simulation as described in §5.1. The simulations of the isolated populations usually produce a much higher spurious fraction (i.e., the number of false-positives divided by the size of the X-ray catalog). For SERVS, VIDEO, CFHTLS, and HSC-PDR1, the median spurious fractions of the isolated populations are 19%, 24%, 30%, and 40%, respectively. For the associated populations, the spurious fractions (defined as $N_{\text{IM}}/(N_{\text{IM}} + N_{\text{CM}})$) for SERVS, VIDEO, CFHTLS, and HSC-PDR1 are 3%, 5%, 7%, and 9%, respectively.

For the MLE matching results of the real data, sources that were not reliably matched to any counterparts (with a total number of N_{negative}) should contain a mixture of the FNs of the associated population and the TNs of the isolated population. Therefore, we can use the median FN and

TN from simulations to estimate the fraction of X-ray sources in the associated population (f_{AP}):

$$N_{\text{negative}} = N_{\text{FN}} \times f_{\text{AP}} + N_{\text{TN}} \times (1 - f_{\text{AP}}). \quad (8)$$

With f_{AP} , we can estimate the expected number of X-ray sources to have a spurious match as the weighted sum of IM and FP. The false matching rate, f_{False} should therefore be:

$$f_{\text{False}} = (N_{\text{IM}} \times f_{\text{AP}} + N_{\text{FP}} \times (1 - f_{\text{AP}}))/(N_{\text{positive}}). \quad (9)$$

Here we consider N_{positive} as the combination of both the “reliable” and “acceptable” matches reported in Table 2. We carry out simulations for each OIR catalog. The values of f_{False} and f_{AP} for each OIR catalog are also reported in Table 2. Due to the high f_{AP} values, the false matching rates of our matching results are mostly determined by the spurious fractions of the associated populations, which are much lower than those of the isolated populations. Notably, adopting the *Chandra*-matched counterpart magnitude density, $q(m)_{\text{Chandra}}$, does reduce the false-matching rates compared to those derived using $q(m)_{\text{XMM-Newton}}$. For the SERVS and VIDEO catalogs, the improvements are marginal (< 0.5%), while the improvements for CFHTLS and HSC-PDR1 are more significant ($\approx 2\%$ and 6%, respectively).

We further scrutinize the MLE matching reliabilities by making use of the 241 CSC sources and their multiwavelength matching results described in §5.1. We assess the reliability of the matching results of these *Chandra* sources using the aforementioned Monte Carlo method, and find that the false-match fractions are 0.9%, 1.4%, 2.8%, and 3.3%, for SERVS, VIDEO, CFHTLS, and HSC-PDR1, respectively. For each catalog, we also directly compare the reliable matches obtained with *XMM-Newton* and *Chandra* positions for these 241 sources, and find that 97%, 94%, 91%, and 87% of the *Chandra* matching results and the *XMM-Newton* results are the same for the SERVS, VIDEO, CFHTLS, and HSC catalogs, respectively. The agreement between the matching results for the *Chandra* sources and those of corresponding *XMM-Newton* sources are consistent with the false-matching rates suggested by the Monte Carlo simulation considering the small number of *Chandra*-detected subsample.

5.3 The NWAY Bayesian catalog matching method

We supplement the MLE matching results with the Bayesian catalog matching tool, NWAY (Salvato et al. 2017).¹⁶ The fundamental difference between the Bayesian approach and the likelihood-ratio approach is that the Bayesian approach makes use of the distance and magnitude priors from multiple catalogs simultaneously to select the most probable match. The details of NWAY’s matching methodology is described in Appendix B of Salvato et al. (2017).

NWAY computes three informative quantities for deciding the most probable match, p_{single} , p_{any} and p_i , where each possible counterpart has a different p_{single} value based on their distance from the *XMM-Newton* position. This value could be weighted by the priors supplied (e.g., $q(m)$ and $n(m)$ in Equation 6 are similar to a magnitude prior). In our case, p_{single} is the posterior probability for a counterpart that is correctly associated with the X-ray source based on the angular separation from the X-ray position weighted by the magnitude distribution prior, and the surface densities of the X-ray and OIR catalogs. For each X-ray source, p_{single} of all possible counterparts are considered to compute a single p_{any} value, which stands for the posterior probability of the X-ray source having any correct counterparts (i.e., $p_{\text{any}} = 0$ if there are no OIR counterparts within the search radius of the X-ray source.) The last quantity, p_i , is the relative probability of a possible counterpart being the correct match. For an X-ray source with multiple possible counterparts, the counterpart with the highest p_i (p_i (Best)) is considered to be the most probable match and is assigned the MATCH_FLAG = 1 flag by NWAY. Counterparts with p_i higher than 50% of p_i (Best) are also flagged by NWAY as MATCH_FLAG = 2.

Similar to our MLE approach, we make use of the *Chandra* sources in the XMM-LSS field to compute the priors of the expected counterparts. We use the “auto” functionality of NWAY with a 1.5'' search radius for defining the “real” counterparts. In addition to the magnitude priors, we also include an additional prior based on the *Spitzer* IRAC color from SERVS, [3.6μm]/[4.5μm]. Since the majority of the X-ray sources are expected to be AGNs, the distinct [3.6μm]/[4.5μm] mid-IR color of luminous AGNs will provide additional discerning powers. For a small number of sources, this additional prior is useful for discerning two adjacent SERVS sources with comparable magnitudes (see the top-right panel of Fig. 14 for illustration).

After computing the magnitude and IRAC color priors using the *Chandra* sources, we run NWAY on the full X-ray catalog with a search radius of 10''. All four OIR catalogs are considered simultaneously. We report the multiwavelength matches with MATCH_FLAG=1,2 in a separate table in the Appendix (Table B) supplementary to the MLE matching results.

Here we also discuss how we estimated the reliability of NWAY matching results. Since NWAY matches all four OIR catalogs simultaneously, we cannot determine the “associated” and “isolated” populations as we did for estimating the spurious matching rates for MLE results using Monte Carlo simulations. Salvato et al. (2017) suggests that the NWAY matching reliability can be determined by a p_{any}

threshold, which is chosen based on re-running NWAY on randomly shifted “fake” X-ray catalogs. However, this approach is equivalent to estimating the spurious matching rates for the isolated population using the Broos et al. (2007) method, which is usually much higher than the results obtained with the two-population approach (see Broos et al., 2007, Xue et al., 2011, and § 5.2 for details). Therefore, we do not adopt any p_{any} thresholds for the NWAY matching results. The NWAY matching results can still be assessed by investigating the CSC-matched subsample of 241 X-ray sources, and we find that the difference between the matching results obtained using *Chandra* and *XMM-Newton* positions with NWAY are consistent with the MLE results described in §5.2.

We also use the 241 *Chandra*-detected subsample to compare the NWAY and MLE results. We focus only on comparing the SERVS counterparts, as the majority of MLE matching results are decided based on the primary counterparts from SERVS. We confirm that all *Chandra* sources have the same SERVS matching results using MLE and NWAY. Therefore, we can use the *Chandra* results obtained with MLE to assess the matching reliability of both MLE and NWAY matching results. We show examples of such comparisons in Fig. 14. We find 95% of the sources have the same matching results from MLE, NWAY, and *Chandra*. A small fraction (two sources) of MLE matching results do not agree with those of *Chandra* but could be recovered by NWAY. On the other hand, two of the NWAY matching results do not agree with the *Chandra* results but could be identified by MLE. Five of the *Chandra* sources have different SERVS counterparts than both MLE and NWAY results. As demonstrated in Fig 14, each of them have multiple counterparts with comparable magnitudes and similar spatial separations from the *XMM-Newton* position. This suggests MLE and NWAY perform similarly for finding SERVS counterparts.

When further scrutinizing the 95% sources with identical SERVS counterparts from MLE, NWAY, and *Chandra*, we find that NWAY cannot identify the correct counterparts in the other three OIR catalogs for a small fraction ($\sim 10\%$) of sources. For instance, one of the X-ray sources has a reliable SERVS counterpart identified by both NWAY and MLE. For the SERVS counterpart, there is only one VIDEO source within the 0.5'' positional error circle of SERVS. For the MLE approach described in § 5.1, the VIDEO source is associated to the correct SERVS counterpart. However, NWAY does not consider this VIDEO sources to be among the most probable combination of counterparts form all four OIR catalogs that were being matched simultaneously. This is likely due to how NWAY computes p_i . When multiple OIR catalogs are taken into account simultaneously, p_i represents the relative probability of counterparts from *all* OIR catalogs being the correct match. In this example, the VIDEO counterpart has an unlikely magnitude according to the VIDEO magnitude prior therefore including the VIDEO source as a correct match would result in a lower p_i compared to the case where the VIDEO source is “absent”. Similar mismatches are also found when comparing the NWAY and MLE matching results for the full *XMM-Newton* catalog. We note that NWAY do not have this behavior when no magnitude or color priors are used. However, NWAY would rely only on the distance-based prior without the in-

¹⁶ <https://github.com/JohannesBuchner/nway>.

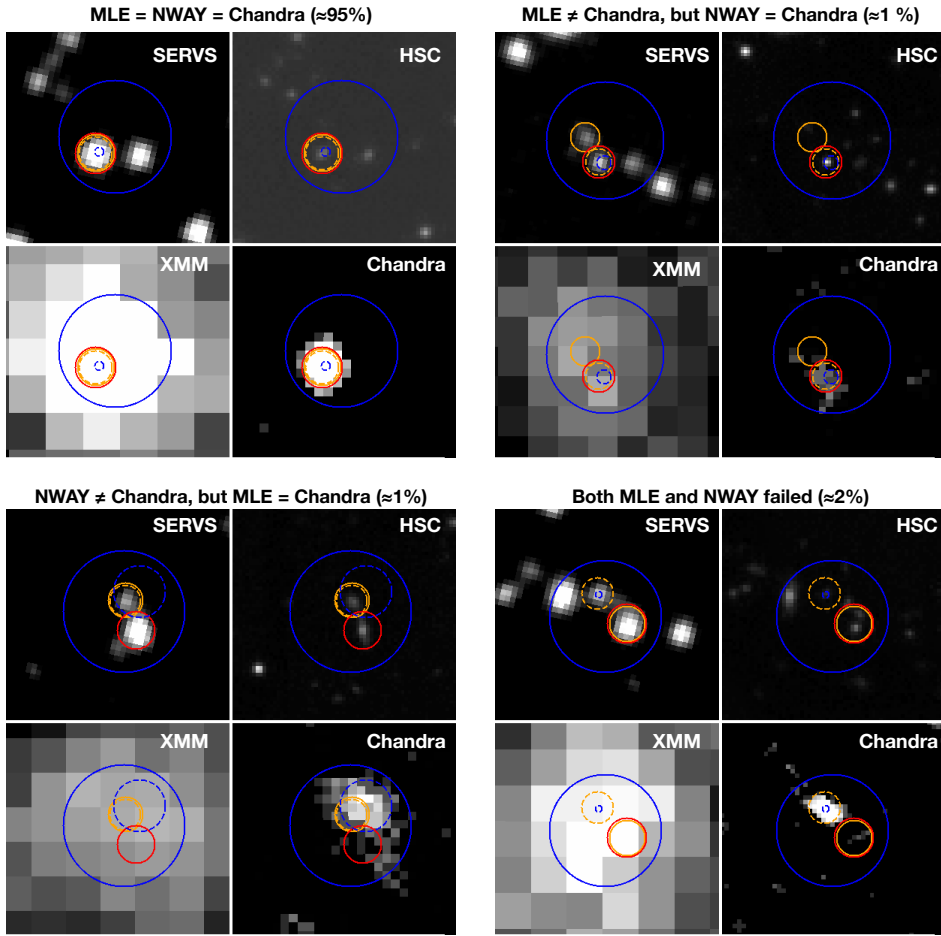


Figure 14. Illustrations of the comparison between the matching results using *XMM-Newton* positions or *Chandra* positions for four X-ray sources in our sample. Within the panel for each source, we show images from SERVS [3.6 μ m](top-left), HSC *i*-band (top-right), *XMM-Newton* 0.5–10 keV (bottom-left), and *Chandra* 0.5–7 keV (bottom-right). X-ray positions are marked as blue circles with a 99% error radius, with the *XMM-Newton* positions marked using solid lines and the *Chandra* positions marked using dashed lines. SERVS counterparts identified with the MLE method are marked as orange circles with a 2'' radius, solid lines mark the counterparts of the *XMM-Newton* positions, and dashed lines mark the counterparts of the *Chandra* positions. SERVS counterparts of the *XMM-Newton* positions identified using NWAY are shown as the red circles. For the vast majority of *XMM-Newton* sources with *Chandra* counterparts from CSC, our counterpart-matching results are identical to the results obtained using *Chandra* coordinates and positional uncertainties.

clusion of magnitude and color priors. Further corroborating the Bayesian method's effectiveness of counterpart-matching with multiple OIR catalogs is beyond the scope of this work. Therefore, we list the NWAY matching results as-is in Table B and we consider only the MLE matching results listed in Table A when exploring the multiwavelength properties in this work.

5.4 Redshifts

The XMM-LSS region is covered by a number of redshift surveys that target galaxies with various optical magnitude constraints, including the PRImus Multi-Object Survey (PRIMUS, Coil et al. 2010), the VIMOS Public Extragalactic Redshift Survey (VIPERS, Garilli et al. 2014), the VIMOS VLT Deep Survey (VVDS, Fevre et al. 2013). As part of the SDSS-BOSS program, 3042 X-ray sources found in the XXL-N field (25 deg^2) with $r < 22.5$ were all

followed-up by SDSS (Menzel et al. 2016). Also, there are three other redshift surveys in the XMM-LSS region that target near-IR selected galaxies, including the spectroscopic follow-up observations of the UKIDSS Ultra-Deep Survey (UDSz, Bradshaw et al. 2013; McLure et al. 2013), the 3D-HST Survey (Skelton et al. 2014; Momcheva et al. 2016) in the UDS region, and the Carnegie-Spitzer-IMACS Redshift Survey (CSI, Kelson et al. (2014)).

We adopt the same nearest-neighbor matching criterion with a 1'' matching radius to associate these redshifts to each OIR catalog. The redshift for each X-ray source is determined by the coordinates of its primary OIR counterpart. In cases where redshifts from different catalogs do not agree with each other, we choose redshifts using the following order (ranked by spectral resolution): SDSS, VVDS, VIPERS, UDSz, PRIMUS (reliable), CSI (reliable), 3D-HST, PRIMUS (acceptable), CSI (acceptable). Of the 5218 sources in our main X-ray source catalogs, 1762 of them have

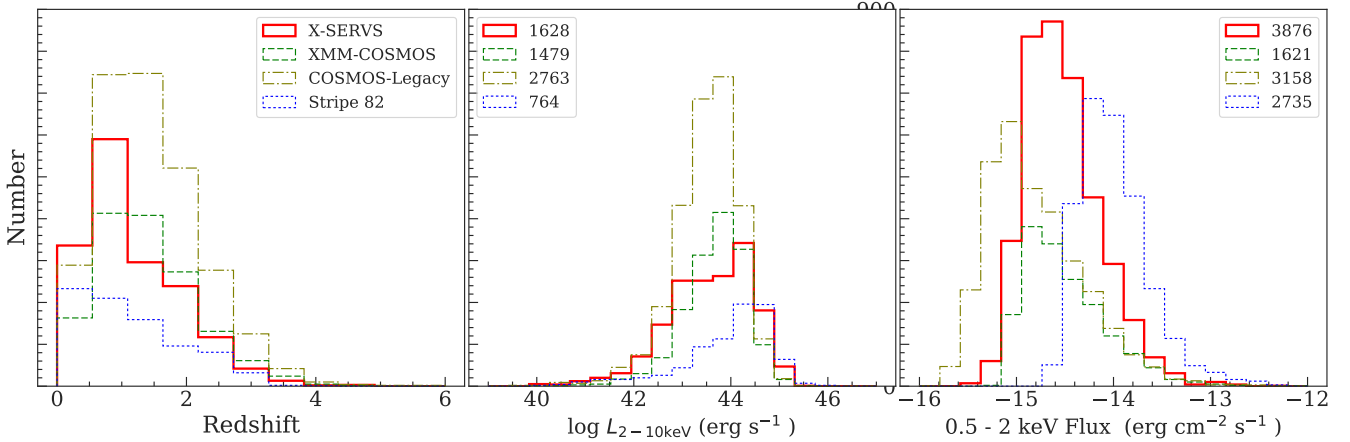


Figure 15. A comparison between this work (solid red line), COSMOS-Legacy (brown dash-dotted line), XMM-COSMOS (blue dotted line), and Stripe 82-X (green dashed line) surveys. Distributions shown in panels from left to right are: redshift, $\log L_{2-10\text{keV}}$, and 0.5–2 keV flux, respectively. For the left and middle panels, the histograms are for the same set of sources with redshift measurements, with source numbers marked in the middle panel. Right panel shows the distribution of soft-band fluxes for the soft-band detected sources in each catalog, no redshift information is required. The numbers of the soft-band sources are also shown in the right panel.

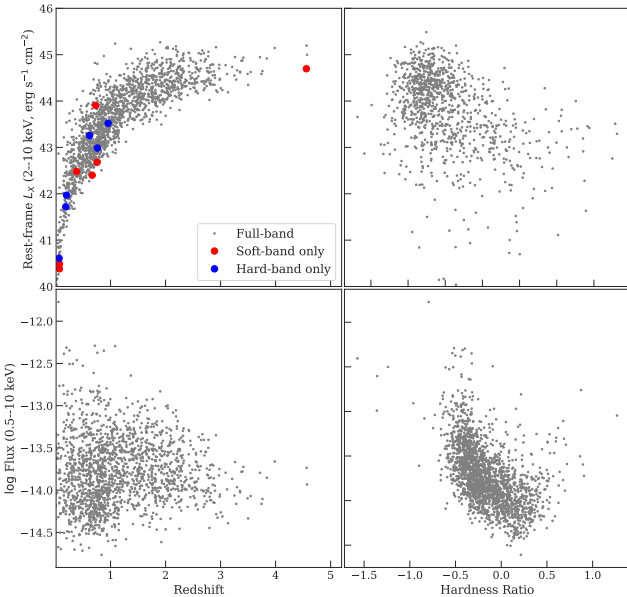


Figure 16. Properties of the 1762 X-ray sources with spectroscopic redshift measurements. Top-left panel shows the $L_{2-10\text{keV}} - z$ distribution, top-right panel shows $L_{2-10\text{keV}}$ vs. hardness ratio. Bottom-left panel shows the distribution of 0.5–10 keV flux vs. redshift. Bottom-right panel shows the distribution of 0.5–10 keV flux vs. hardness ratio.

spectroscopic redshifts ranges from $0.002 < z < 7.01$. We list the properties and the relevant numbers of each redshift catalogs in Table 5.4.

5.5 Source properties and classification

In this section we discuss the properties of the 4854 sources with reliable or acceptable counterparts. For the X-ray sources with a secure redshift, we calculate their rest-frame

Table 3. Redshift catalogs used in this work. Column 1: Redshift survey name. Column 2: Survey instrument. Column 3: Survey sensitivity Column 4: Total number of redshifts assigned to the X-ray sources in the main catalog.

Catalog	Instrument	Survey sensitivity	N_X
3D-HST	WFCS G141 Grism	$JH_{\text{IR}} \lesssim 24$	5
CSI	IMACS (Uniform Dispersion Prism)	$[3.6\mu\text{m}]_{\text{AB}} \lesssim 21$	57
PRIMUS	IMACS (Low-Dispersion Prism)	$i \lesssim 23.5$	364
SDSS	BOSS	$r \lesssim 22.5$	1104
UDSz	VIMOS/FORS2	$K < 23$	17
VVDS	VIMOS	$17.5 \lesssim i \lesssim 24.75$	43
VIPERS	VIMOS	$i \lesssim 22.5$	172

2–10 keV luminosity assuming a $\Gamma = 1.7$ power-law and corrected for the Galactic absorption. We compare the luminosity, flux, and redshift distributions of our sample to those from archival X-ray surveys, including XMM-COSMOS, COSMOS-legacy, and Stripe 82X surveys. We show the comparison in Fig. 15. The comparisons in the middle and right panels are limited to the availability of spectroscopic redshifts in Stripe-82 and XMM-LSS regions. We note that high-quality photometric redshifts are already available in a $\approx 1 \text{ deg}^2$ area within the XMM-LSS region (Nyland et al. 2017). The photometric redshift catalog for the full survey region will also be available soon (Pforr et al., in preparation). Nonetheless, the left-panel of Fig. 15 demonstrates that our catalog occupies a unique parameter space in X-ray surveys by more than doubling the source counts of the XMM-COSMOS survey, which will enable a wide range of science that was previously limited by either survey sensitivity or cosmic variance. For our sample, the $L_X - z$ distribution is shown in Fig. 16, along with the L_X vs. HR, HR vs. Redshift, and full-band flux vs. Redshift distributions.

We also include the basic source classifications in our catalog. For sources with spectroscopic observations, we directly make use of the spectroscopic classifications when

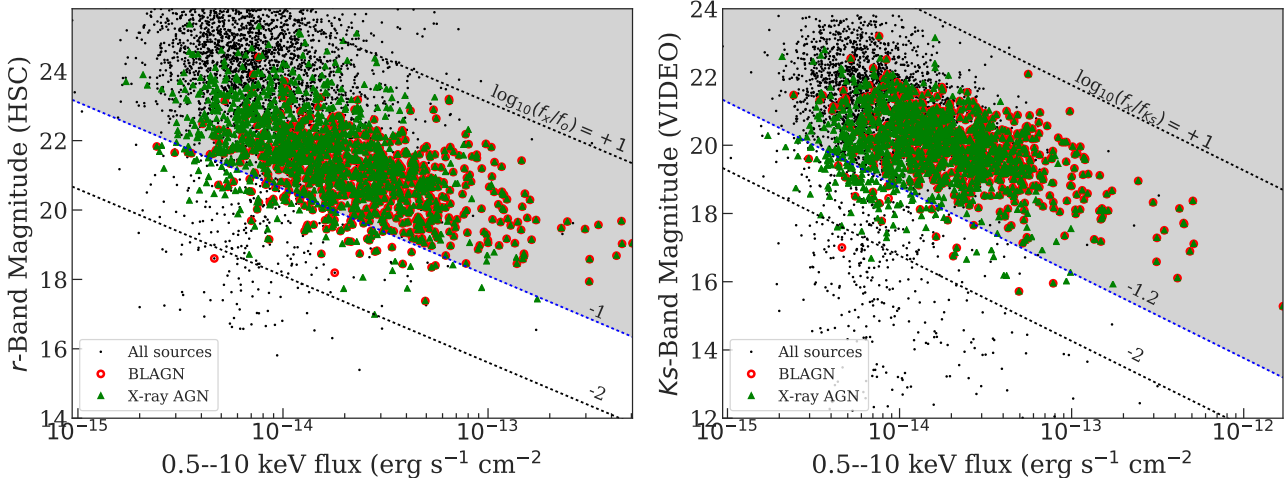


Figure 17. Right – Distributions of the full-band (0.5–10 keV) X-ray flux and the optical flux at r -band. Left – Full-band X-ray flux versus the near-IR flux at K_s -band. In both plots, the shaded regions mark the “AGN” regime as defined by the $\log_{10} f_x/f_o > -1$ (right) or the $\log_{10} f_x/f_{Ks} > -1.2$ (left) thresholds as described in §4.4 of Xue et al. (2011). For sources with spectroscopic redshift measurements, we also make those with $L_X > 3 \times 10^{42}$ erg cm $^{-2}$ s $^{-1}$ as the green triangles. Source that are identified as broad-line AGNs are also marked as open red circles.

available. A total of 831 sources are classified as AGNs based on the presence of the broad lines in their optical spectra from SDSS, VIPERS, or VVDS. For the other sources, we use the criteria described in Luo et al. (2017) to select AGNs, including: 1. A X-ray luminosity threshold where we regard sources with rest-frame $L_{2-10\text{keV}} > 3 \times 10^{42}$ erg s $^{-1}$ as an AGN. A total of 1504 sources satisfy this criteron. 2. X-ray bright sources with X-ray-to-optical and X-ray-to-near-IR flux ratios larger than $\log f_x/f_R > -1$ and $\log f_x/f_{Ks} > -1.2$, respectively. There are 3409 sources with $\log f_x/f_R > -1$ and 4071 sources with $\log f_x/f_{Ks} > -1.2$. The total number of sources classified as AGN is 4584, or $\approx 88\%$ of the total sample. We show the flux ratio distributions in Fig. 17.

6 CATALOG DESCRIPTION

Here we describe the columns of the main X-ray source catalog, Table 7. Null values are filled with -99.

1. Column 1: the unique source ID (XID) assigned to each X-ray source.
2. Columns 2–3: RA and DEC in degrees of the X-ray source.
3. Column 4. X-ray positional uncertainty (σ_x) in arcthat this is not the σ of Gaussian distribution but rather the scaling parameter of the univariate Rayleigh distribution (see §3.3 and Pineau et al. (2017) for details). The positional uncertainties are based on those of the full-band. For sources without a full-band detection, the soft or hard-band positional uncertainties are used.
4. Columns 5–6: 68% and 99.9% X-ray positional uncertainties in arcsec, see §3.3 for details.
5. Columns 7–14: RA/DEC in degrees of the source at the soft-band, hard-band, and full-band, respectively.
6. Columns 15–18: DET_ML at different bands.
7. Columns 23–34: Exposure times in seconds (total, PN, MOS1, MOS2) at different bands.
8. Columns 35–50: Value of the background map (counts per pixel) at different bands.
9. Columns 51–58: Source counts at different bands (PN+MOS)
10. Columns 59–66: Total count rates at different bands.
11. Columns 67–78: Source counts at different bands for PN, MOS1, and MOS2.
12. Columns 79–90: Count rates at different bands for PN, MOS1, and MOS2. In count s $^{-1}$.
13. Columns 91–98: Flux and flux uncertainty (error-weighted average of different EPIC detectors) for different bands. In erg cm $^{-2}$ s $^{-1}$.
14. Columns 99–101: Hardness ratio and its upper and lower limits.
15. Columns 102: Rest-frame 2–10 keV X-ray luminosity
16. Columns 103–106: Number of sources within the 99% positional uncertainties.
17. Columns 107–110: Number of sources that satisfies $LR \geq LR_{\text{th}}$.
18. Column 111: Whether an X-ray source has at least one reliable counterpart with $LR > LR_{\text{threshold}}$ from any of the four OIR catalogs.
19. Column 112: Whether an X-ray source has no reliable counterparts but has at least an acceptable counterpart from any of the four OIR catalogs (see §5 for details).
20. Column 113: Whether an X-ray source has no reliable or acceptable counterparts.
21. Column 114: Whether an X-ray source has no counterparts from any of the four OIR catalogs.
22. Column 115: Catalog from which the primary counterpart is selected.
23. Column 116–118: RA, DEC of the primary counterpart and its separation from the X-ray source.
24. Column 119: The matching likelihood ratio.
25. Columns 120–124: The same as Columns 114–118, but for the secondary counterpart (only if the secondary counterpart is also reliable, see §5.1 for details).
26. Columns 125–129: The same as Columns 114–118, but for

- the tertiary counterpart (only if the tertiary counterpart is also reliable).
27. Columns 130–141: RA, DEC, and Object ID from the original OIR catalog for the primary counterpart.
 28. Columns 142–153: Same as Columns 126–137 but for the secondary counterpart.
 29. Columns 154–165: Same as Columns 126–137 but for the tertiary counterpart.
 30. Columns 166–167: SERVS 3'' aperture photometry at $3.6\mu\text{m}$ and $4.5\mu\text{m}$.
 31. Columns 167–171: SWIRE 3'' aperture photometry at $3.6\mu\text{m}$, $4.5\mu\text{m}$, $5.8\mu\text{m}$, and $8.0\mu\text{m}$.
 32. Columns 172–181: VIDEO psf photometry Y , J , H , and Ks -band magnitude and uncertainties.
 33. Columns 182–191: CFHTLS PSF photometry at u , g , r , i , z bands.
 34. Columns 192–201: HSC cmodel photometry at g , r , i , z , y bands.
 35. Columns: 202–204: RA, DEC, and Object ID from the original redshift catalogs for the primary counterparts.
 36. Column 205: Redshift.
 37. Column 206: The catalog from which the redshift is culled from.
 38. Column 207: Original redshift flag from one of the redshift catalogs. For SDSS, see <http://www.sdss.org/dr14/algorithms/bitmasks/#ZWARNING>. For VVDS, see §3.4 of Fevre et al. (2013). For VIPERS, see §4.3 of Garilli et al. (2014). For PRIMUS, see <http://primus.ucsd.edu/version1.html#ztags>. For CSI, see §4.6 of Kelson et al. (2014). For UDSz, see McLure et al. (2013). For the 3D-HST catalog, we only select redshifts with $\sigma_z/(1+z) \leq 0.003$ thus no redshift flags are included.
 39. Column 208: Source classification. See §5.5 for details.

We also include a supplementary table for the matching results by NWAY. The columns of Table 7 are listed below. The first-half of the table presents the matching results that included magnitude priors for each OIR catalog and a prior of IRAC color for SERVS.

1. Column 1: the unique source ID (XID) assigned to each X-ray source.
2. Columns 2–13: RA, DEC, separation to the X-ray position, and the original Object ID of the matched counterpart from each OIR catalog.
3. Column 14: p_i
4. Column 15: p_{any}
5. Column 16: p_{single}
6. Column 17: MATCH_FLAG. The most probable counterparts have MATCH_FLAG=1. Other counterparts that are almost as good have MATCH_FLAG=2.

For each source, we also generate postage-stamp images in the X-ray, mid-IR, near-IR, and optical wavelengths. For illustration, we show a random collection of 16 sources in Figure 18.

7 SUMMARY

In this work, we present a new X-ray source catalog in the XMM-LSS region constructed with both archival and *XMM-Newton* AO-15 data. We summarize the main results as the following:

1. Our X-ray catalog is constructed based on data in a ≈ 5.3 deg 2 rectangular region centered at RA=35.58°, DEC=−4.965°. A total of 153 pointings from 149 different *XMM-Newton* obsIDs are used, with a total of ≈ 2.7 Ms background-filtered exposure time (1.1 Ms from AO-15).
2. The main X-ray source catalog is generated using the Ewavelet and EMLDETECT. We list all 5218 sources with EMLDETECT DET_ML > 6 in either the soft-band (0.5–2 keV), hard-band (2–10 keV), or the full-band (0.5–10 keV). Of the 5218 sources, we find 2843 of them to be the same X-ray sources identified in previous X-ray surveys in our survey area (the XXL-N surveys, Liu et al. 2016) and 2375 are newly discovered X-ray sources.
3. The median fluxes in $\text{erg cm}^{-2} \text{s}^{-1}$ for the three X-ray bands are 2.7×10^{-15} (0.5–2 keV), 1.5×10^{-14} (2–10 keV), 8.8×10^{-15} (0.5–10 keV). There are 2928 sources with more than 100 X-ray counts in full-band (PN + MOS), and 126 sources with more than 1000 X-ray counts.
4. Monte Carlo simulation suggests that the number of spurious sources should be ≈ 41 with a DET_ML=6.0 threshold, which is $\approx 99.2\%$ reliable. If we raise the detection threshold to DET_ML=10.8, or 99.8% reliability, and the expected number of spurious sources would be 12.
5. The absolute astrometry of the *XMM-Newton* catalog is registered to the WCS frame of the Subaru HSC-PDR1 survey. The positional uncertainties for the X-ray sources are determined based on an empirical relation between the X-ray-to-optical positional offsets and the X-ray source counts, which is well-characterized by the Rayleigh distribution. The median positional uncertainties at the soft, hard, and full-bands are: 1.31'', 1.35'', and 1.37'', respectively.
6. We search for OIR counterparts in SERVS, VIDEO, CFHTLS, and HSC-PDR1 surveys and we find that 99.5% (5196/5218) of the X-ray sources have at least one OIR counterparts within the 99% positional uncertainties. We also find that $\approx 93\%$ (4854/5218) of the X-ray sources have at least one reliable OIR counterpart. We also collect 1762 secure redshifts from SDSS, VIPERS, VVDS, UDSz, PRIMUS, CSI, and 3D-HST.
7. We test the matching results using a subsample of 241 X-ray sources with a reliable *Chandra* counterpart from CSC 2.0. We find that $\approx 96\%$ of the matching results from *XMM-Newton* and *Chandra* are identical, suggesting our multi-wavelength matching results are highly reliable.
8. We classify 4584 X-ray sources as an AGN. The classification is based on their optical spectral from SDSS, VIPERS, or VVDS (831); X-ray luminosity larger than $3 \times 10^{42} \text{ erg cm}^{-2} \text{s}^{-1}$ (1504); and large X-ray-to-optical and X-ray-to-NIR flux ratios (4479).

The X-SERVS:XMM-LSS source catalogs presented in this work will provide the first step in understanding the details of the relation between AGN evolution and environment over the largest cosmic structure different from the existing COSMOS datasets. In the near future, the inclusion of COSMOS, deeper *Chandra* survey in Boötes, and additional X-ray surveys of similar depth and high-quality multiwavelength coverages can further increase the AGN sample size and will allow for a better understanding of the relation between different large-scale structures and AGN evolutions.

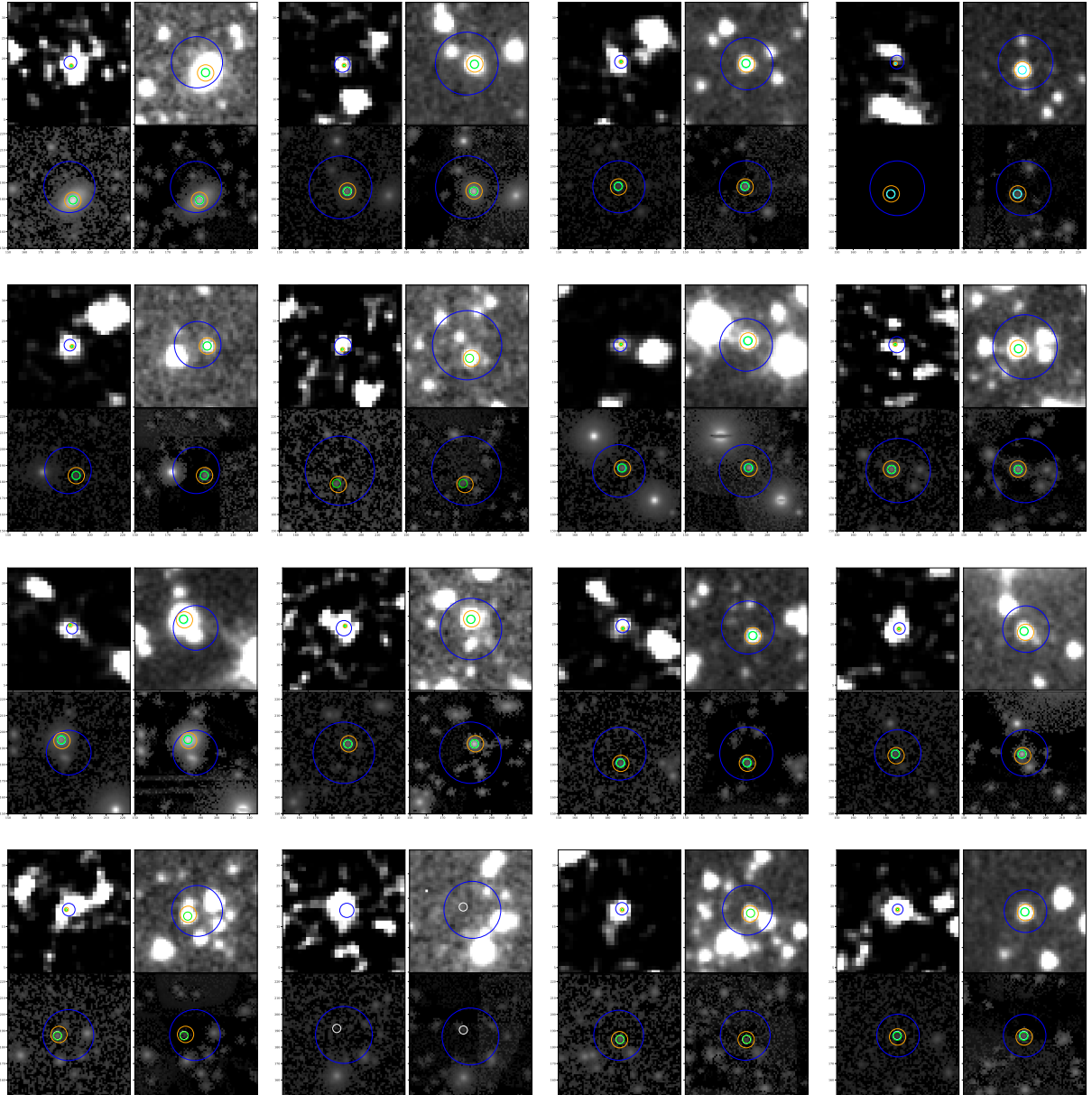


Figure 18. Postage-stamp images for 16 randomly selected X-ray sources. For each source, we show 1. X-ray image (upper-left panel) 2. mid-IR image from SERVS (upper-right panel) 3. near-IR image from VIDEO (lower-left panel) 4. optical image from HSC-PDR1 (lower-right panel). In each image, the X-ray position is marked as the blue circle with the corresponding 99% error radius. The position of the most probable mid-IR counterpart is marked as the orange circle with a 2'' radius. The positions of VIDEO, CFHTLS, and HSC-PDR1 counterparts are marked as 1'' circles of green, cyan, and white colors, respectively. The entire set of postage-stamp images are available online.

ACKNOWLEDGMENTS

To be completed We acknowledge the support of NASA grant NNX17AF07G (CTC, WNB). This work is based on observations taken by the 3D-HST Treasury Program (GO 12177 and 12328) with the NASA/ESA HST, which is operated by the Association of Universities for Research in Astronomy, Inc., under NASA contract NAS5-26555.

Funding for PRIMUS is provided by NSF (AST-0607701, AST-0908246, AST-0908442, AST-0908354) and NASA (Spitzer-1356708, 08-ADP08-0019, NNX09AC95G).

NAOJ / HSC Collaboration

This paper uses data from the VIMOS Public Extragalactic Redshift Survey (VIPERS). VIPERS has been performed using the ESO Very Large Telescope, under the "Large Programme" 182.A-0886. The participating institutions and funding agencies are listed at <http://vipers.inaf.it>

This research uses data from the VIMOS VLT Deep Survey, obtained from the VVDS database operated by Cefam, Laboratoire d'Astrophysique de Marseille, France.

SDSS :
CSI :

Table A. The main X-ray source catalog with a selection of columns. Empty or null values are marked as -99. The numbers listed on the second row of this table is the column number of the full X-ray catalog with 208 columns. See §6 for a detailed descriptions of each column. This table is available in its entirety in machine-readable form online.

XID (1)	RA (2)	DEC (3)	σ_x (4)	FB.DET_ML (15)	FB.EXP (23)	FB.BKG (35)	FB.SCTS (51)	FB.FLUX (91)	HR (99)	$L_{2-10keV}$ (102)	LR.FLAG.RE (111)	LRA.CATALOG (115)	LRA.ZBEST (205)	LRA.ZSOURCE (206)	CLASS (208)
XMM00000	34.200218	-4.035255	1.44	19.0	59076.2	1.74	83.04	8.3e-15	-99	-99	False	SERVS	-99	-99	AGN
XMM00001	34.200713	-4.933734	1.45	63.0	61051.8	1.0	82.03	7.93e-15	-99	8.983e+43	True	SERVS	1.82	UDSz	AGN
XMM00002	34.201454	-5.556716	1.96	16.4	29731.6	0.8	29.64	5.31e-15	-99	2.46e+42	True	SERVS	0.459	VIPERS	AGN
XMM00003	34.201466	-4.499315	1.5	23.3	72553.8	1.76	72.37	5.32e-15	-99	1.37e+43	True	SERVS	0.959	PRIMUS	AGN
XMM00004	34.201949	-4.555523	0.93	316.8	87846.9	1.81	351.91	2.666e-14	-0.43	9.57e+42	True	SERVS	0.41	SDSS	AGN
XMM00005	34.202636	-5.690719	1.66	16.5	26430.1	1.01	52.23	1.301e-14	-99	1.6854e+44	True	CFHTLS	1.932	VIPERS	AGN
XMM00006	34.203276	-4.315289	1.55	29.2	107957.7	1.79	65.42	2.94e-15	-99	-99	True	SERVS	-99	-99	AGN
XMM00007	34.203748	-5.433790	1.77	11.3	78270.8	1.54	41.87	4.71e-15	-99	-99	True	VIDEO	-99	-99	AGN
XMM00008	34.203820	-4.595275	1.17	114.8	83485.0	1.49	168.25	1.214e-14	-0.48	2.05e+42	True	VIDEO	0.294	SDSS	AGN
XMM00009	34.204668	-5.378238	1.35	57.1	93769.9	1.4	101.92	6.8e-15	-99	-99	False	SERVS	-99	-99	AGN
XMM00010	34.204772	-4.520794	1.51	32.0	77664.5	1.51	71.54	5.7e-15	-99	-99	True	SERVS	-99	-99	AGN
XMM00011	34.206732	-4.469321	1.25	81.2	63040.8	1.74	132.09	1.579e-14	-99	2.61e+42	True	SERVS	0.291	SDSS	AGN
XMM00012	34.207426	-4.585313	1.54	17.3	94203.8	1.85	67.16	4.22e-15	-99	6.8e+41	True	SERVS	0.289	PRIMUS	
XMM00013	34.208245	-5.295083	1.28	66.6	91655.9	1.22	124.63	7.18e-15	-0.32	-99	True	SERVS	-99	-99	AGN
XMM00014	34.209443	-4.012790	1.34	34.8	63642.5	1.92	106.5	9.3e-15	-99	-99	True	SERVS	-99	-99	AGN
XMM00015	34.209479	-4.028269	0.88	349.3	68619.6	1.94	426.86	4.119e-14	-0.12	1.2566e+44	True	SERVS	1.031	SDSS	AGN
XMM00016	34.209496	-4.421868	1.48	89.5	23041.3	0.22	76.5	2.309e-14	-99	0.0	True	SERVS	0.0	SDSS	
XMM00017	34.209799	-4.328703	1.12	84.6	115477.7	2.71	194.51	1.317e-14	-99	2.17e+42	True	SERVS	0.291	SDSS	AGN
XMM00018	34.209992	-4.563673	1.14	187.9	88839.2	1.41	181.45	1.38e-14	-0.25	-99	True	SERVS	-99	-99	AGN
XMM00019	34.210413	-3.890166	1.53	37.9	44730.1	0.95	68.48	7.55e-15	-99	-99	True	CFHTLS	-99	-99	AGN
XMM00020	34.210863	-5.410119	1.76	11.6	89369.8	1.53	43.01	2.63e-15	-99	-99	True	SERVS	-99	-99	AGN
XMM00021	34.211423	-5.194363	1.09	104.2	85216.5	1.93	207.87	1.356e-14	-0.36	1.58e+42	True	SERVS	0.249	SDSS	
XMM00022	34.211535	-3.892733	1.62	-99	-99	-99	-99	-99	-99	-99	False	HSC	-99	-99	
XMM00023	34.211690	-5.313163	1.44	34.3	96622.2	1.24	83.2	4.54e-15	-99	4.33e+42	True	SERVS	0.627	VIPERS	AGN
XMM00024	34.213193	-4.355747	1.64	11.1	100517.8	2.9	54.4	4.4e-15	-99	-99	True	SERVS	-99	-99	AGN
XMM00025	34.214208	-5.417995	1.75	10.7	88372.6	1.56	43.75	5.35e-15	-99	-99	True	SERVS	-99	-99	AGN
XMM00026	34.215117	-4.937388	1.82	13.5	64067.0	1.07	38.16	5.06e-15	-99	-99	True	SERVS	-99	-99	AGN
XMM00027	34.215205	-4.388650	1.73	16.5	67996.2	2.29	45.43	3.98e-15	-99	4.7e+41	True	SERVS	0.251	PRIMUS	
XMM00028	34.215240	-3.918303	1.62	15.1	33523.0	0.94	56.51	6.71e-15	-99	-99	True	SERVS	-99	-99	AGN
XMM00029	34.217465	-4.087917	1.48	22.2	82858.6	1.96	75.51	6.05e-15	-99	7.65e+42	True	SERVS	0.707	PRIMUS	AGN
XMM00030	34.217481	-5.601158	1.71	17.5	24629.1	1.0	47.25	1.061e-14	-99	7.024e+43	True	VIDEO	1.44	SDSS	AGN

Table B. The NWAY matching results with a selection of columns. Empty or null values are marked as -99. See §6 for a detailed descriptions of each column.

XID	NWA_PANY	NWA_PI	NWA_SERVS_ID	NWA_SERVS_MAG1	NWA_VIDEO_ID	NWA_VIDEO_KSMAG	NWA_CFHT_ID	NWA_CFHT_IMAG	NWA_HSC_ID	NWA_HSC_IMAG
XMM00000	0.99	0.96	172727	20.5	644245983190	21.08	1114.031255	21.93	37484971320960508	22.04
XMM00001	0.94	1.0	-99	-99	644245946363	17.51	1123.223188	19.29	37484833882002514	19.22
XMM00002	1.0	0.99	174016	17.13	644245975018	17.08	1114.024092	17.85	-99	-99
XMM00003	0.99	0.6	172557	19.57	644245974364	19.35	1114.023481	20.58	37485108759912843	20.5
XMM00004	0.99	0.97	130124	18.41	644245971200	18.41	1114.021145	19.78	37484833882008818	19.85
XMM00005	0.99	0.98	-99	-99	-99	-99	1123.211260	20.41	37484692148084612	20.56
XMM00006	0.99	1.0	-99	-99	-99	-99	1123.212886	20.98	37484692148084849	21.09
XMM00007	1.0	0.99	159785	19.4	644245968189	20.16	1114.018595	21.27	37485108759911057	21.16
XMM00008	0.15	0.37	-99	-99	644245967227	19.97	-99	-99	-99	-99
XMM00009	0.94	1.0	-99	-99	644246423098	19.85	1114.015512	20.02	-99	-99
XMM00010	0.56	0.67	-99	-99	644245971580	21.66	1114.021242	22.87	37484971320960299	21.79

REFERENCES

- Aihara H., et al., 2017, arXiv eprint: 1702.08449
- Bradshaw E. J., et al., 2013, *Mon. Not. R. Astron. Soc.*, 433, 194
- Brandt W. N., Alexander D. M., 2015, *Astron. Astrophys. Rev.*, 23, 1
- Broos P. S., Feigelson E. D., Townsley L. K., Getman K. V., Wang J., Garmire G. P., Jiang Z., Tsuboi Y., 2007, *Astrophys. J. Suppl. Ser.*, 169, 353
- Broos P. S., et al., 2011, *Astrophys. J. Suppl. Vol. 194, Issue 1, Artic. id. 2, 19 pp. (2011)*, 194
- Brusa M., et al., 2007, *Astrophys. J. Suppl. Ser.*, 172, 353
- Cappelluti N., et al., 2007, *Astrophys. J. Suppl. Ser.*, 172, 341
- Cappelluti N., et al., 2009, *Astron. Astrophys.*, 497, 635
- Chiappetti L., et al., 2005, *Astron. Astrophys.*, 439, 413
- Coil A. L., et al., 2010, *Astrophys. Journal, Vol. 741, Issue 1, Artic. id. 8, 15 pp. (2011)*, 741
- Evans I. N., et al., 2010, *Astrophys. J. Suppl. Ser.*, 189, 37
- Fevre O. L., et al., 2013, *Astron. Astrophys.*, 559, A14
- Garilli B., et al., 2014, *Astron. Astrophys.*, 562, A23
- Hudelot P., et al., 2012, VizieR On-line Data Cat. II/317. Orig. Publ. SPIE Conf. 2012, 2317
- Jarvis M. J., et al., 2013, *Mon. Not. R. Astron. Soc.*, 428, 1281
- Kelson D. D., et al., 2014, *Astrophys. J.*, 783, 110
- Kim M., Wilkes B. J., Kim D., Green P. J., Barkhouse W. A., Lee M. G., Silverman J. D., Tananbaum H. D., 2007, *Astrophys. J.*, 659, 29
- LaMassa S. M., et al., 2016, *Astrophys. J.*, 817, 172
- Liu Z., et al., 2016, *Mon. Not. R. Astron. Soc.*, 459, 1602
- Lonsdale C. J., et al., 2003, *Publ. Astron. Soc. Pacific, Vol. 115, Issue 810, pp. 897-927.*, 115, 897
- Luo B., et al., 2010, *Astrophys. J. Suppl. Ser.*, 187, 560
- Luo B., et al., 2017, *Astrophys. J. Suppl. Ser.*, 228, 2
- Marchesi S., et al., 2016, *Astrophys. J.*, 817, 34
- Mauduit J. C., et al., 2012, *Publ. Astron. Soc. Pacific, Vol. 124, Issue 917, pp. 714 (2012)*, 124, 714
- McLure R. J., et al., 2013, *Mon. Not. R. Astron. Soc.*, 428, 1088
- Menzel M. L., et al., 2016, *Mon. Not. R. Astron. Soc.*, 457, 110
- Momcheva I. G., et al., 2016, *Astrophys. J. Suppl. Ser.*, 225, 27
- Pacaud F., et al., 2006, *Mon. Not. R. Astron. Soc.*, 372, 578
- Pierre M., et al., 2016, *Astron. Astrophys.*, 592, A1
- Pineau F.-X., et al., 2017, *Astron. Astrophys.*, 597, A89
- Ranalli P., et al., 2013, *Astron. Astrophys.*, 555, A42
- Ranalli P., et al., 2015, *Astron. Astrophys.*, 577, A121
- Rosen S. R., et al., 2016, *Astron. Astrophys.*, 590, A1
- Salvato M., et al., 2017, arXiv eprint: 1705.10711
- Skelton R. E., et al., 2014, *Astrophys. J. Suppl. Ser. Vol. 214, Issue 2, Artic. id. 24, 49 pp. (2014)*, 214, 214
- Sutherland W., Saunders W., 1992, *Mon. Not. R. Astron. Soc.*, 259, 413
- Ueda Y., et al., 2008, *Astrophys. J. Suppl. Ser.*, 179, 124
- Vaccari M., 2016, Proc. "The many Facet. extragalactic radio Surv. Towar. new Sci. challenges" (EXTRA-RADSUR2015). 20-23 Oct. 2015. Bol. Italy. Online <http://pos.sissa.it/cgi-bin/reader/conf.cgi?confid=267, id.27>
- Watson M. G., et al., 2008, *Astron. Astrophys.*, 493, 339
- Xue Y. Q., et al., 2011, *Astrophys. J. Suppl. Ser.*, 195, 10

This paper has been typeset from a TeX/LaTeX file prepared by the author.